



Wind–wave characterization and modeling in the Azores Archipelago

Nuno M.R. Monteiro^{a,*}, Tiago C.A. Oliveira^a, Paulo A. Silva^a, Ali Adbolali^{b,c}

^a Physics Department & Centre of Environmental and Marine Studies, University of Aveiro, 3810-193, Aveiro, Portugal

^b NWS/NCEP/Environmental Modeling Center, National Oceanic and Atmospheric Administration (NOAA), College Park, MD, USA

^c University of Maryland, College Park, MD, USA

ARTICLE INFO

Keywords:

WAVEWATCH III
Unstructured mesh
Hurricane
Islands
Spectral wave model
Coastal
EMODnet

ABSTRACT

Wind–wave characterization and modeling around a group of islands can have significant challenges due to strong diffraction, shoaling, and reflection. In this work, the wind–wave climate of the Azores archipelago (North Atlantic Ocean) is characterized based on wave buoy measurements recorded between 2012 and 2021 at five different locations with water depth ranging from 80 to 110 m. Moreover, wave measurements during four storms of extratropical origin and two storms of tropical origin are analyzed in detail. Due to identified island shadow effects, the average significant wave height (H_s) ranged between 1.50 m (S. Miguel island) and 1.86 m (Graciosa island) in the south and north of the archipelago, respectively. Under storm conditions, shadow effects can lead to differences up to approximately 7 m in H_s between the north and south of the archipelago. The ability to simulate the local wave conditions by an unstructured WAVEWATCH III model covering the north Atlantic with high resolution around the Azores Archipelago is analyzed. In addition, the model performance and scalability on two different High Performance Computing environments are analyzed considering different numerical schemes and parallelization algorithms.

1. Introduction

Wind–wave characterization and modeling in coastal areas around islands still present significant challenges (e.g., [Violante-Carvalho et al., 2021](#); [Mentaschi et al., 2020](#); [Gonçalves et al., 2020](#); [Sun et al., 2019b](#); [Andrefouet et al., 2012](#)). These challenges can be due to the lack of field wave data recorded around islands or the difficulty of using numerical models capable of accurately solving wave diffraction, reflection, and refraction around islands. In addition, wind–wave models can still confront difficulties representing realistic ocean environments due to the lack of accurate topographic data ([Adbolali et al., 2020](#)), inaccurate atmospheric forcing in the coastal areas ([Adbolali et al., 2021](#); [Ma et al., 2020](#)), exclusion of water level and current fields from ocean circulation and hydrological models ([Bakhtyar et al., 2020](#); [Moghimi et al., 2020](#)), coarse resolution of model grid ([Bakhtyar et al., 2020](#); [Moghimi et al., 2020](#); [Adbolali et al., 2020](#)), or simplification in the parametrization of dominant physics in coastal areas in the model ([Adbolali et al., 2021](#)).

The Azores Archipelago is located in the central North Atlantic and exposed to the North Atlantic wave climate. Consequently, the archipelago presents high seasonal wave variability ([Morales-Márquez et al., 2020](#); [Dodet et al., 2010](#)) and receives energetic wind–wave storms associated with storms of extratropical and tropical origin ([Campos et al., 2022a](#); [Oliveira et al., 2020a](#); [Andrade et al., 2008](#)). The

wave climate in the Azores islands has been studied for several practical applications. These studies include the evaluation of the spatial distribution and seasonal variation of wave energy ([Gonçalves and Soares, 2020](#); [Matos et al., 2015](#); [Rusu and Soares, 2012](#)), analyzing beach morphodynamics ([Lafon et al., 2005](#)), coastline and shelf position as they result from induced wave erosion ([Quartau et al., 2012](#)), and evaluating risk assessment related to wave overtopping and flooding scenarios ([Fortes et al., 2020](#)). These analysis relied on observations (e.g., [Esteves et al., 2009](#); [Andrade et al., 2008](#)) and hindcast data (e.g., [Rusu and Soares, 2012](#); [Dodet et al., 2010](#); [Pontes et al., 1996](#)).

The numerical simulation of wave generation and propagation with spectral wave models constitutes a powerful tool for analyzing the current wave climate, overcoming the spatial and temporal limitations of buoy and satellite altimeter data. The scientific community has been using the WAVEWATCH III (WW3, hereinafter) third-generation spectral wave model ([WW3DG, 2019](#)) to simulate wind–waves from global (e.g., [Brus et al., 2021](#); [Stopa et al., 2016](#)) to regional scales, including hindcast (e.g., [Sheng et al., 2019](#); [Sun et al., 2019b](#); [Dodet et al., 2010](#)), forecast (e.g., [Campos et al., 2022a](#); [Brus et al., 2021](#); [Oliveira et al., 2020b](#); [Chawla et al., 2013](#)), and climate projections (e.g., [Casas-Prat and Wang, 2020](#); [Morim et al., 2019](#)). The traditional method

* Corresponding author.

E-mail addresses: nunom@ua.pt (N.M.R. Monteiro), toliveira@ua.pt (T.C.A. Oliveira), psilva@ua.pt (P.A. Silva), ali.abdolali@noaa.gov (A. Adbolali).

to simulate waves with WW3 in high-resolution mode has been using multi-grid models (e.g., Campos et al., 2022b; Chawla et al., 2013; Dodet et al., 2010). In these cases, one or several regional grids are often nested inside a larger and coarser-resolution grid (Tolman, 2008). However, multi-grid models require demanding time step restrictions for coastal resolutions to ensure numerical stability, increasing the computational cost.

The unstructured grid version of WW3 (with triangular elements) is an alternative to multi-scale resolution modeling (Brus et al., 2021; Adbolali et al., 2021, 2020; Mentaschi et al., 2020; Sun et al., 2019a; Roland, 2009). The unstructured grid models have been employed in WW3 using numerical schemes based on residual contour distribution (Roland, 2012). These numerical schemes allow running the model on high resolution near coasts and islands. For the explicit scheme, the CFL condition must be fulfilled to guarantee a stable integration in the space domain (WW3DG, 2019). One advantage of the explicit schemes is that they are faster than the implicit schemes for the same time step, because explicit schemes require a single equation to evaluate new variables for a single time step. Adbolali et al. (2020) implemented the implicit scheme in WW3 (at resolutions up to 10 m) with a new parallelization algorithm introduced to the model (domain decomposition). This implementation presented better performances than the explicit solver while also being scalable for a high number of CPU cores. However, the explicit scheme is still efficient for a coarse unstructured mesh, which does not require a small time step. On the other hand, when a high resolution unstructured mesh is used (with 10 m or higher resolution), a very small time step is needed and it is not possible to use the explicit scheme efficiently. Here, the implicit scheme is the alternative (Adbolali et al., 2020).

The new model implementation introduced in Adbolali et al. (2020) is a breakthrough for the scientific community since there is an increasing need for high-resolution nearshore wave modeling with better computational performances (e.g., Adbolali et al., 2021; Mentaschi et al., 2020). Furthermore, even for lower resolution meshes (global to regional scales), the WW3 unstructured model has been shown to have a lower computational cost than a WW3 structured model (Brus et al., 2021).

Tools to easily change WW3 meshes according to the areas of interest are vital to moving classical multi-grid to unstructured mesh models. Indeed, recent development in open-source meshing software like OceanMesh2D (Roberts et al., 2019), for Matlab, have been successfully used to create optimized unstructured meshes for WW3 in an automatic way (e.g., Brus et al., 2021). The use of OceanMesh2D with WW3 could, for example, help in studies dealing with small islands' vulnerability to sea-level rise (e.g., Enríquez et al., 2017; Connell, 2015; Hearty and Neumann, 2001), as high resolution wind-wave simulations are required.

There is also an increasing need for long-term (order of decades) wind-wave simulations for hindcast and future wave climate projection studies. Therefore, efficient computational resources, combined with efficient meshes and state-of-the-art numerical models, are pivotal for faster and high-quality results. Consequently, there has been an increase in High Performance Computing (HPC) resources used for wind-wave simulations. However, HPC resources cost can be significant and, therefore, it is vital to understand computational performances and scalability of wind-wave models.

The main goals of this paper are: (i) to characterize the nearshore wind-wave climate of the Azores archipelago based on long-term nearshore in-situ measurements; (ii) to identify and characterize energetic wind-wave storm events in the in-situ measurements; (iii) to model mean and storm wind-waves conditions with high-resolution near the Azores archipelago using an unstructured WW3 model; (v) to study the performance and the scalability of the unstructured WW3 model in two different HPC environments considering different numerical and parallelization algorithms.

The mean wave and storm conditions characterization uses in-situ measurements from five nearshore wave buoys in the Azores Archipelago, recorded between 2012 and 2021. The aim is to understand if the wave distribution patterns around the archipelago and island shadow effects are similar during normal and storm conditions. For the wind-wave model, the Matlab version of OceanMesh2D was utilized to create a mesh with spatial scales ranging from around 55 km down to 50 m. The WW3 unstructured model was validated using in-situ measurements in a time span of approximately 20 months. In addition, an analysis of the nearshore storm conditions was performed based on model results. Multiple simulation tests were performed in the HPC environments BOB (<https://macc.fcn.pt/resources>) and ARGUS (<https://www.ua.pt/pt/stic/computacao>) to study the computational performance and scalability of the model. This analysis used different model setups, with two parallelization algorithms (card deck and domain decomposition) and two numerical model schemes (explicit and implicit).

After this introductory section, the study area and wind-wave buoy data used in this work are presented in Section 2. Wind-waves in the Azores Archipelago are characterized in Section 3 based on buoy data analyses. Next, Section 4 presents the implementation of the wind-wave model. Section 5 presents the wind-wave model results, performance, and scalability. A discussion of the results obtained in this study is provided in Section 6. Finally, Section 7 summarizes the main findings.

2. Study area and wind-wave data

2.1. The Azores Archipelago

The Azores Archipelago is located in the North Atlantic Ocean, in the Mid-Atlantic Ridge at approximately 1500 km from Continental Europe (see Fig. 1a) and is the result of volcanic activity. It is formed by nine islands, distributed along 600 km and divided into three groups (Fig. 1b): the Occidental group (Flores and Corvo), the Central group (Terceira, Graciosa, São Jorge, Pico e Faial) and the Oriental group (Santa Maria and São Miguel). The seafloor surrounding the islands is characterized by very narrow shelves and steep slopes. The tidal pattern in the Azores is semidiurnal, with a tidal range of less than 1 m (Quartau et al., 2012).

2.2. Wind-wave buoy data

In-situ wind-wave measurements from five directional wave buoys around the Azores Archipelago islands are used (Fig. 1). These buoys provide wave parameters based on 10 min long record of sea-surface elevation with a sampling frequency of 1.28 Hz, and are from the CLIMAAT project (Azevedo and Gonçalo, 2005) of the University of Azores, supported by ECOMARPORT (<https://ecomarport.eu/>). The data from these wave buoys is freely available based on the European Union effort of providing access to the observations made by individual organizations in all Member States, mainly through the European Marine Observation and Data Network (EMODnet, <https://emodnet.ec.europa.eu>).

The wind-wave parameters available for the five buoys are the following: (i) $H_{1/3}$ (or H_s): Average of 1/3 highest wave heights (also known as *significant wave height*); (ii) H_{gs} : Generic significant wave height; (iii) H_{max} : Maximum zero crossing wave height; (iv) T_{max} : Maximum wave period; (v) T_{hmax} : Period of the highest wave; (vi) T_z : Mean zero crossing wave period; and (vii) Dir : Mean wave direction relative to true North (clockwise). This paper analyzes H_s , H_{max} , T_z , and Dir data at the five buoys from 2012/05/01 at 00:00 (hereafter all times in UTC 00:00) to 2021/02/28 at 23:50 UTC for the characterization of mean conditions (full wave buoy datasets) and storm conditions.

The geographical location of the buoys is shown in Fig. 1b, and general information about them is summarized in Table 1. The buoys

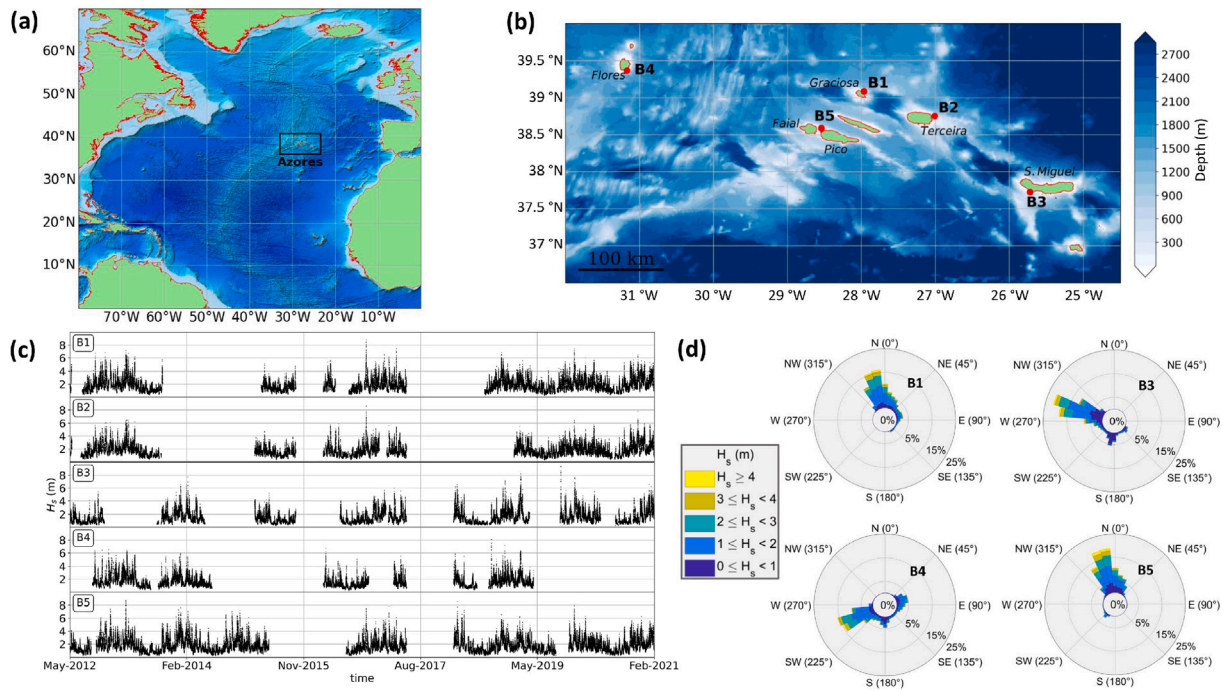


Fig. 1. Top maps display (a) the location of the Azores Archipelago, and (b) the bathymetry in the vicinity of Azores and the location of the wave buoys. On the bottom, (c) H_s time series for all wave buoys and (d) wave-roses for all buoys (except B2), displaying the distribution of H_s in function of 10° Dir bins. (For interpretation of the references to color in this figure legend, the reader is referred to the web version of this article.)

Table 1

Characteristics of the studied wave buoys.

Buoy name (EMODNET ID)	Latitude	Longitude	Depth (m)	Distance to coast (km)	Number of sea states	Percentage of missed sea states
B1 (6202400)	39.087°N	27.962°W	97	2.3	288 687	39.52%
B2 (6202401)	38.751°N	27.010°W	100	3.6	242 707	49.16%
B3 (6202402)	37.726°N	25.721°W	90	1.5	267 465	43.97%
B4 (6202403)	39.364°N	31.167°W	80	1.0	174 147	63.52%
B5 (6202404)	38.587°N	28.538°W	110	4.1	353 710	25.90%

are named in this work as: B1 (northeast of Graciosa island), B2 (northeast Terceira island), B3 (near the city of Ponta Delgada in S. Miguel island), B4 (south of Flores island), and B5 (Faial-Pico channel). B1, B2 and B5 are located in the central group, B3 in the Eastern group, and B4 in the Western group of the archipelago. On average, the buoys are located at 2.5 km from the coast (see Table 1), with B4 being the closest to the coast (1.0 km) and B5 the farthest (4.1 km). The depth of the wave buoys ranges between 80 m (B4) and 110 m (B5). The periods where the buoys were measuring simultaneously can be observed in Fig. 1c, which shows the complete time series of H_s for the five buoys.

In general, long term wave buoy measurements display some missing data (e.g., Mendes and Oliveira, 2021; Oliveira et al., 2018), due to rough wave conditions during major storms, ship collisions or buoy maintenance periods. Buoy B4 has the highest percentage of missed sea states (64.52%), while B5 is the buoy that preserves the most sea states within the largest possible timeframe, with only 25.90% of lacking data (see Fig. 1c and Table 1). Considering all the buoys, the missing data correspond to 44.41%. These values are higher than 20% found for coastal wave buoys (Oliveira et al., 2018) and 34% for deep water buoys (Mendes and Oliveira, 2021) in Portugal mainland. With this significant amount of missed data, some periods of time were not surveyed: (i) the Summer of 2014, where there was no data except for B5; (ii) the Winter of 2015, where all buoys lacked data; and (iii) a period from June to October 2017, where all buoys lacked data.

3. Wind-wave characterization

3.1. Mean wave conditions

Table 2 contains basic statistics of H_s , H_{max} , T_z and Dir at the five buoys, for global (January to December), winter (December to March) and summer (June to September) conditions. Under global conditions, the means of H_s range between 1.50 m (B3) and 1.86 m (B1), the means of H_{max} range between 2.31 m (B3) and 2.83 m (B1). For summer conditions, the minimum recorded mean values in H_s and H_{max} were 0.92 m and 1.44 m respectively, both at B3. For winter conditions, the maximum recorded mean values of H_s and H_{max} were 2.28 m and 3.44 m respectively, both at B1. Moreover, standard deviations of H_s and H_{max} were the highest (1.03 m and 1.53 m respectively) at B5, under global conditions.

For global mean conditions, T_z mean values ranged between 6.1 s (B1) and 7.0 s (B4). The absolute maximum of T_z (accounting for all buoys) happened at 2017/02/27 in B5, with a value of 16.6 s. On that same day, the absolute maximums at B1 (15.3 s) and B2 (16.4 s) were also reached. Furthermore, the means of T_z range between 5.6 s (B4) and 6.2 s (B1 and B2) for summer, and between 6.5 s (B4) and 7.7 s (B1) for winter. The mean of T_z standard deviations was 1.3 s and 1.4 s, for summer and winter conditions respectively.

Wave-roses representing the H_s distribution in function of 10° Dir bins (for B1, B3, B4 and B5) are presented in Fig. 1d. The wave-roses depict different preferential wave directions at each buoy, as a consequence of island shadow effects. Wave buoy B1 and B5 are more exposed to the incoming wind-waves from northwest, while B3 and

Table 2

Wind–waves general statistics at the five buoys in Azores. Mean and standard deviation values are given for global conditions (GC, January to December), winter conditions (WNT, December to March), and summer conditions (SMR, June to September).

Significant wave height (H_s) [m]									
Buoy	Mean			Standard deviation			Min.	Max.	Date of maximum
	GC	WNT	SMR	GC	WNT	SMR			
B1	1.86	2.28	1.30	0.96	0.94	0.65	0.03	9.05	2016/10/24 00:30
B2	1.79	2.17	1.26	0.87	0.85	0.55	0.29	8.75	2016/10/23 22:40
B3	1.50	2.05	0.92	0.96	1.04	0.49	0.06	10.06	2019/10/02 14:50
B4	1.64	2.11	1.15	0.88	0.92	0.64	0.08	8.10	2018/09/15 21:30
B5	1.75	2.21	1.08	1.03	1.03	0.62	0.12	9.74	2013/03/08 17:43
Maximum wave height (H_{max}) [m]									
Buoy	Mean			Standard deviation			Min.	Max.	Date of maximum
	GC	WNT	SMR	GC	WNT	SMR			
B1	2.83	3.44	2.01	1.45	1.43	0.99	0.06	14.93	2016/10/23 00:30
B2	2.72	3.30	1.94	1.32	1.31	0.85	0.43	14.28	2015/02/25 02:21
B3	2.31	3.13	1.44	1.46	1.59	0.77	0.08	16.47	2019/10/02 12:40
B4	2.52	3.22	1.78	1.35	1.41	0.99	0.16	12.92	2018/09/15 23:10
B5	2.67	3.34	1.67	1.53	0.99	0.94	0.25	14.95	2019/12/15 14:30
Mean zero-crossing wave period (T_z) [s]									
Buoy	Mean			Standard deviation			Min.	Max.	Date of maximum
	GC	WNT	SMR	GC	WNT	SMR			
B1	7.0	7.7	6.2	1.5	1.4	1.2	2.7	15.3	2017/02/27 18:40
B2	6.8	7.4	6.2	1.4	1.4	1.1	3.3	16.4	2017/02/27 18:00
B3	6.3	6.9	5.9	1.3	1.4	1.1	3.1	14.4	2021/01/31 14:20
B4	6.1	6.5	5.6	1.1	1.1	1.0	3.3	12.7	2018/06/07 09:00
B5	6.8	7.5	5.9	1.6	1.6	1.3	2.9	16.6	2017/02/27 13:40
Direction relative to true North (Dir)									
Buoy	Mean [°N]			Standard deviation [°]					
	GC	WNT	SMR	GC	WNT	SMR			
B1	211	244	189	151	140	151			
B2	–	–	–	–	–	–			
B3	257	266	243	50	47	51			
B4	189	209	186	72	59	69			
B5	245	268	223	143	129	151			

B4, located south of S. Miguel and Flores Island, respectively, mainly depict waves from the W and SW. Dir data for B2 is not shown in the wave-roses of Fig. 1, and will not be analyzed, because it was erratic (for unknown reasons) and clearly does not represent the wind–wave climate of the region.

Mean values of Dir range between 189°N (B4) and 257°N (B3) under normal conditions, 186°N (B4) and 243°N (B3) under summer conditions, and 209°N and 268°N under winter conditions. Also, buoys B1 and B5 generally present a high standard deviation (151° and 143°, respectively, under global conditions) compared to B3 (50°) and B4 (72°).

Standard deviation values of H_s , H_{max} and T_z were the lowest at buoy B4. This could be due to the significant amount of missing sea states at B4 (63.52%), compared to the other four buoys (the second highest was 49.16%, in B2), as shown in Table 1.

3.2. Storm events

Six wind–wave storm events that reached the Azores archipelago are studied in more detail in this work. The six storm events were named here as S_a (October 2012), S_b (March 2013), S_c (October 2016), S_d (October 2019), S_e (March and April 2020) and S_f (November 2020). These events were selected based on three conditions: (i) due to their severity; (ii) simultaneous detection in two or more of the five buoys; and (iii) variety of weather systems (extratropical and tropical storms) that triggered the different wind–wave storms. The best tracks of the storm centers are shown in Fig. 2. For the systems with tropical origin (S_a and S_d), the best tracks were directly obtained from the National Hurricane Center (<https://www.nhc.noaa.gov/data/#hurdat>).

For the extratropical storms, the best tracks were obtained based on the minimum surface pressure locations from ERA5 data (Hersbach et al., 2020).

Storm S_a corresponds to the post-tropical storm Rafael, coming to the Azores from the northwest (Avila, 2013). Rafael was a category one hurricane in the Saffir–Simpson scale (Simpson and Saffir, 1974; Saffir, 1973), reaching maximum sustained wind speeds of 148 km/h and a minimum pressure center of 969 mb at 2012/10/16, 12:00, south of Bermuda, and arrived to Azores six days later, under *extratropical cyclone* classification, reaching maximum sustained winds of 74 km/h there (Avila, 2013).

S_d was hurricane Lorenzo, which, at its intensity peak, reached a minimum central pressure of 937 mb and maximum sustained winds of 232 km/h. When Lorenzo's pressure center crossed near the western islands of Azores, at October 2, it was a category 1 (Saffir–Simpson) hurricane, and the storm left the archipelago by the end of October 3, already as an extratropical storm (Zelinsky, 2019). Wind gusts at Faial and Flores islands reached a peak of 145 km/h and 142 km/h, respectively. Significant damages occurred in the Azores, primarily on Flores and Corvo Islands. The commercial port of Lajes on Flores Island was destroyed. At the same time, downed trees and power lines caused power outages across both islands (Zelinsky, 2019).

Storm S_f was storm Clement (extratropical storm), named by AEMET (<http://www.aemet.es/>) on 27 November, that mainly affected the western and central groups of Azores, and was part of the 2020–2021 European storm season. Finally, three of the identified wind–wave storms (S_b , S_c , and S_e) were unnamed extratropical cyclones, even though it is worth mentioning that the maximum of H_s registered in B1, B2 and B5 during the S_c event were among the highest absolute values of those in-situ datasets, as will be seen later in the paper.

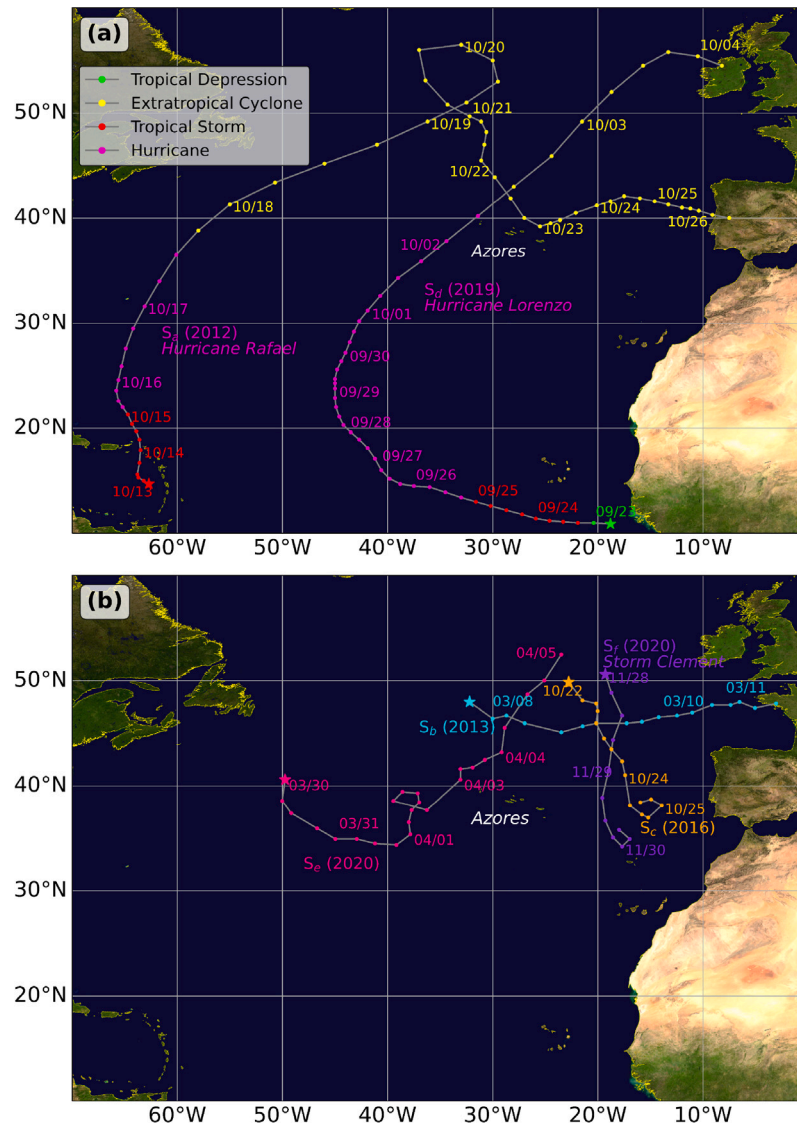


Fig. 2. Tracks of the low pressure centers of the studied storm events for (a) the two storms of tropical origin (S_d and S_d) and (b) the storms of extratropical origin (S_b , S_c , S_e and S_f). The star symbols denote the beginning of the storm tracks. For the storms of tropical origin, track colors denote the storm stages according to Saffir-Simpson scale, based on the maximum sustained wind speeds. (For interpretation of the references to color in this figure legend, the reader is referred to the web version of this article.)

To evaluate if wind-wave storm conditions were reached at all the five buoys during the six storm events, a significant wave height threshold was used (H_{thres}). Wind-wave storm conditions were considered if during the storm event $H_s > H_{thres} = 2 \cdot \overline{H_s}$ (where $\overline{H_s}$ is the mean of H_s recorded in a given buoy). This threshold definition follows a wave storm identification metric proposed in Boccotti (2000), which is characterized as the average value of H_s multiplied by 1.5, but this constant can be higher (2 or 3), depending on the studied wave climate (Lafage et al., 2015). Furthermore, IH (Hydrographic Institute, Portugal) identifies wave storms in the buoys located in the mainland west and south coasts of Portugal with roughly the same metric used here (Mendes and Oliveira, 2021). Moreover, a minimum time of 12 h between two consecutive and independent storms was considered as an independence storm criterion (Oliveira et al., 2018).

Average and maximum values of H_s and T_z during the storms are shown in Table 3. In the same table, the average, minimum and maximum values of Dir (except for buoy B2), and the storm detection thresholds at each buoy (H_{thres}) are also shown. For non wind-wave storms cases, the statistical values of the wind-wave parameters were

calculated based on the period starting in the first instant, t_0 , to the last instant, t_f , where a wind-wave storm was detected, from all buoys (first column of Table 3).

For the six storms, the recorded H_s maximums were 9.05 m at B1 (S_c , at 2016/10/24), 8.75 m at B2 (S_c , at 2016/10/24), 10.06 m at B3 (S_d , at 2019/10/03), 3.40 m for B4 (S_b , at 2013/09/08), and 9.74 m for B5 (S_b , at 2013/09/08). Moreover these H_s maximums recorded during the 6 storms correspond to the absolute maximums of B1, B2, B3, and B5 datasets (see Table 2). Also, the maximums of H_{max} at B1 (S_c) and B3 (S_d) correspond to the absolute maximum values at each of the buoys.

The island shadow effect promotes the reduction of the storm wave energy at some of the wave buoys. For example, the wave height of incoming northern waves were highly reduced for B3, which is located at 2.5 km from the south coast of S. Miguel Island. This was observed for the extratropical storms (winter storms), with the case of events S_d , S_c and S_f , where generally in B1, B2, B4 and B5 much higher waves were observed than in B3. The highest difference in the maximum values of H_s on these situations was 7.03 m (during the extratropical

Table 3

Generic characterization (means and extreme values) of the wind–wave parameters at the five buoys for the six atmospheric storm events. For buoys that reach wind–wave storm conditions, results are shown in bold style.

Event (t_0 /duration)	Buoy	H_{lres} [m]	$\overline{H_s}/\max(H_s)$ [m] (date of max.)	$\overline{T_z}/\max(T_z)$ [s]	$\overline{Dir}/\min(Dir)/\max(Dir)$ [°N]
S_a (2012/10/21, 15:00/59 h)	B1	3.72	4.45/6.08 (10/22, 23:10)	9.7/12.4	348/326/359
	B2	3.58	3.95/5.11 (10/22, 22:34)	10.2/12.7	–
	B3	3.00	3.08/3.27 (10/23, 04:49)	7.5/8.4	292/283/300
	B4	3.28	1.32/2.08 (10/23, 12:56)	5.7/8.4	186/0/354
	B5	3.50	4.88/7.30 (10/22, 23:40)	9.7/13.0	343/325/354
S_b (2013/03/07, 14:00/67 h)	B1	3.72	5.01/7.36 (09/09, 17:45)	9.58/12.3	224/0/359
	B2	3.58	4.64/7.91 (09/09, 18:47)	9.8/12.8	–
	B3	3.00	–	–	–
	B4	3.28	3.34/3.40 (09/08, 04:30)	7.8/8.2	248/240/256
	B5	3.50	5.36/9.74 (09/09, 17:43)	9.7/13.0	311/0/359
S_c (2016/10/22, 03:00/72 h)	B1	3.72	5.46/9.05 (10/24, 00:30)	8.1/11.3	149/0/359
	B2	3.58	5.21/8.75 (10/24, 22:39)	8.1/11.6	–
	B3	3.00	1.98/2.92 (10/23, 05:30)	6.3/7.8	304/287/325
	B4	3.28	1.63/3.27 (10/23, 05:20)	6.3/9.0	81/34/282
	B5	3.50	4.98/8.21 (10/24, 03:10)	8.2/12.1	188/1/359
S_d (2019/10/02, 03:00/31 h)	B1	3.72	4.08/4.87 (10/02, 09:10)	9.5/11.0	337/329/343
	B2	3.58	2.77/3.43 (10/02, 03:00)	7.5/10.1	–
	B3	3.00	5.29/10.06 (10/03, 14:50)	9.5/12.7	254/240/301
	B4	3.28	–	–	–
	B5	3.50	–	–	–
S_e (2020/03/30, 16:00/81 h)	B1	3.72	4.49/5.83 (04/01, 15:10)	8.1/10.8	66/37/108
	B2	3.58	4.46/5.80 (04/01, 21:39)	8.1/10.3	–
	B3	3.00	3.34/4.24 (04/02, 04:30)	6.6/7.6	144/132/159
	B4	3.28	–	–	–
	B5	3.50	3.67/3.74 (03/31, 05:20)	8.3/8.8	40/18/96
S_f (2020/11/27, 19:00 /67 h)	B1	3.72	4.55/6.98 (11/30, 14:50)	8.1/11.0	134/0/359
	B2	3.58	4.64/7.88 (11/29, 10:30)	8.1/11.5	–
	B3	3.00	1.58/2.43 (11/29, 06:30)	5.8/7.5	293/3/347
	B4	3.28	–	–	–
	B5	3.50	4.09/5.32 (11/29, 08:20)	8.2/9.6	203/1/359

storm S_c), between B1 (in the north) and B3 (in the south). However, for subtropical storms coming from southwest typically, there was an opposite effect where B3 measured higher waves than B1 and B2. That was the case of hurricane Lorenzo (event S_d), with B1 and B2 getting significantly lower H_s maximums than B3, up to a difference of 6.63 m.

4. Wind–wave model

4.1. WAVEWATCH III model

The WAVEWATCH III (or WW3) model version 6.07 (WW3DG, 2019) was implemented to simulate wind–waves in the North Atlantic with high resolution around the Azores archipelago. WW3 is a state-of-art third-generation spectral wave model widely used in wave forecasts/hindcasts, which solves the wave action equation, based on the spectral energy balance equation in the Eulerian form (WW3DG, 2019). More specifically, this equation describes the linear propagation of action density spectrum, with additional physical effects (e.g., refraction) and other parameter definitions accounted by source terms in Eq. (1). The simplified version of the spectral energy balance equation used in WW3 is the following:

$$\frac{DN}{Dt} = \frac{S}{\sigma} \quad (1)$$

where N is the action density spectrum, σ is the phase frequency, and S is the net effect of the source terms described by:

$$S = S_{in} + S_{inl} + S_{nl} + S_{ds} + S_{bot} + S_{db} + S_{tr} + S_{sc} + S_{ice} + S_{ref} + S_{user} \quad (2)$$

where the source terms on Eq. (2) are: (i) S_{in} , linear input; (ii) S_{inl} , input term (generally dominated by the exponential wind–wave growth term); (iii) S_{nl} , nonlinear wave–wave interactions; (iv) S_{ds} , wave–ocean interaction term (generally dominated by wave breaking); (v) S_{bot} , wave–bottom interactions; (vi) S_{db} , additional breaking term for shallow waters; (vii) S_{tr} , triad wave–wave interactions; (viii) S_{sc} , scattering

of waves by bottom features; (ix) S_{ice} , wave–ice interactions; (x) S_{ref} , reflections due to coastlines or floating objects (e.g. icebergs); (xi) S_{user} , additional user defined source terms. Note that some of these terms are optional.

The source terms are selected through the use of model switches. The set of switches (which comprise a switch file required when compiling the model in a machine) controls mathematical and physical model definitions (e.g. source terms and propagation schemes), and software options (processor type, parallel computing options, etc.). In this paper, all the WW3 simulations considered the same set source terms. The main model source terms and their respective switches are listed in Table 4.

The WW3 unstructured model was used, discretized with a single mesh that has high-resolution near the Azores islands (down to ~50 m), in spherical coordinates. The explicit and implicit numerical schemes of the model were implemented. Regarding the CPU core parallelization algorithms, with an MPI implementation, used in two HPC systems, the card deck algorithm (used by default in WW3) and the domain decomposition algorithm, applied with the MPI-based parallel library ParMETIS (Karypis and Kumar, 1998), were both used. The three used model setups for the performance and scalability analysis were: (i) explicit and card-deck (EXP CD, hereinafter), (ii) explicit and domain decomposition (EXP DD, henceforward), and (iii) implicit domain decomposition (IMP DD, hereinafter). The purpose was to compare the performances of WW3 for these three configurations of the model but also to assess and analyze the model scalability for up to 1000 cores in the studied HPC environments (ARGUS-HPC and BOB-HPC).

Long WW3 simulations were performed for three time intervals: 2016/09/01 to 2017/01/01, 2018/10/01 to 2019/01/01, and 2020/01/01 to 01/01/2021. The five buoys were recording data almost all the time during these three periods, which was the main reason to simulate them. In addition, three time periods were simulated to study the wind–waves generated by S_a , S_b , and S_d (referred in Section 3.2):

Table 4

Main source terms used in WW3 for all wind-wave simulations on this study.

Source term (s)	Switch parameter	Characteristics
S_{nl}	NL1	Discrete interaction approximation (DIA)
S_{in} and S_{ds}	ST4	Source term from Ardhuin et al. (2010)
S_{bot}	BT4	SHOWEX bottom friction formulation
S_{db}	DB1	Formulation from Battjes and Janssen (1978)

(i) from 2012/10/19 to 2012/10/25, for S_a , (ii) from 2013/03/06 to 2013/03/12, for S_b , (iii) from 2019/09/30 to 2019/10/05, for S_d . The wind-wave model data of the storms S_c (2016), S_e (2020) and S_f (2020) were extracted from the three long simulations described before. Moreover, the output wind-wave parameters in all simulations were (i) H_s , (ii) T_{02} (mean wave period based on 0th and 2nd moment of the spectrum), which is an estimate of T_z , and (iii) Dir .

4.2. Meshing

To generate the triangular unstructured mesh which represents the 2D space-domain of the wind-wave model, the OceanMesh2D (OM2D) software (version 4.0) for Matlab ([Roberts et al., 2019](#)) was used. OM2D has a state-of-the-art mesh generation algorithm ([Koko, 2015](#)), which creates Delaunay triangulations and handles well highly complex geometries of coastlines, as mesh boundary conditions. All generated grids with OM2D are always valid within the Galerkin finite element framework, so that the numerical methods in WW3 are functional, and mesh quality optimizations are also made, i.e. how equilateral the triangles are, which is evaluated through a quality metric threshold, to ensure numerical stability ([Bank, 1998](#)). The complete workflow of OM2D and WW3 is summarized in a flowchart in [Fig. A.1 \(Appendix A\)](#).

The resulting optimized unstructured mesh (from now on, called m_A) has 36 222 nodes and 66 436 elements ([Fig. 3](#)), with resolution ranging from ~55 km down to ~50 m. The areas with greater edge resolutions are located in the vicinity of the Azores islands. Moreover, the mesh smoothness, i.e. how fast is the variations between the smallest and largest edge sizes (defined by the OM2D *grade* parameter), is greater around the Azores Archipelago, to ensure there is great resolution along smaller island channels and that complex wind-wave phenomena on islands are well represented.

There is an option in OM2D that allows for the creation of fixed nodes if a set of coordinates is given. Five points containing the coordinates (see [Table 1](#)) of the studied wave buoys in Azores were set as fixed in mesh m_A , so that the model validation in the next chapters is as accurate as possible. Regarding the mesh coastlines (green polygons) near the archipelago (see [Fig. 3c](#) to [g](#)), it is possible to notice that they are not always matching with the input coastlines (red lines) do match due to the lack of bathymetric resolution in nearshore regions, showing portions of land areas where there was supposed to be sea (more noticeable in maps [e](#)) and [f](#)) of [Fig. 3](#).

4.3. Coastline and bathymetry

Coastline data from GSHHG – Global Self-consistent, Hierarchical, High-resolution Geography Database (<https://www.soest.hawaii.edu/pwessel/gshhg/>) – were used, which contains five different datasets with different coastline spatial resolutions. Only two datasets of GSHHG were considered: (i) the full resolution, with resolutions up to ~100 m, and (ii) the coarse resolution, with resolutions up to ~10 km. The finer resolution dataset was used to represent the region around the Azores Archipelago (see the red lines, showing these coastlines, in [Fig. 3](#)), while the coarser resolution dataset served the purpose of depicting the remaining coastlines in the North Atlantic.

Two bathymetry datasets were used: (i) DEM_1 : from the *GEBCO 2020* global bathymetry dataset from the General Bathymetric Chart of the Oceans (GEBCO) with 15 arc-second resolution (~450 m) ([Tozer](#)

[et al., 2019](#)) developed by the Nippon-Foundation, and (ii) DEM_2 : a bathymetry model, with a resolution of 50 m, compiled with high-resolution data from several multibeam surveys but also with less refined single-beam data. While DEM_1 encompasses the North Atlantic and the eastern and western islands in Azores, DEM_2 represents the bathymetry of the central region of the archipelago (Graciosa, Faial, Pico and Terceira islands). On a side note, in the Azores islands' coastal regions inside DEM_2 geographical limits (maps [c](#)), [d](#)) and [g](#)) of [Fig. 3](#), the mesh coastlines overlap much more with the input coastlines (GSHHG) than the coastal regions outside DEM_2 (maps [e](#) and [f](#) of [Fig. 3](#)). This is due to higher resolution of DEM_2 dataset, which leads to a better mesh representation in nearshore areas.

For DEM_2 (see [Fig. 4](#)), the bathymetry measurements around Graciosa Island are a compilation ([Quartau et al., 2015](#)) from the MARCHE cruise's multibeam bathymetry ([Miranda et al., 2014](#)), multibeam bathymetry from EMEPC (<https://www.emepc.pt/>) and single-beam bathymetry from EMODNet. The multibeam bathymetry in the inner shelf of Terceira Island was surveyed with a GeoSwath interferometric sonar operating at 250 kHz. Terceira Island's outer shelf and slope bathymetry were obtained with a Simrad EM 710. Both of the last two surveys were implemented under the project Features of Azores and Italian Volcanic Islands ([Quartau et al., 2014](#)). High-resolution bathymetry of the outer shelf and slope of the Faial, Pico and São Jorge Island ([Mitchell et al., 2008, 2003](#)) was acquired in 2003 with a Reson 8160 multibeam sonar system (50 kHz). In the western inner shelf area of Pico and inner shelf of Faial, high-resolution bathymetry was acquired in 2004 with a Submetrix 2000 phase-measuring swath sonar (117 kHz) which covered areas shallower than 80 m water depth ([Tempera, 2008](#)). The remaining shelf gaps of Faial and Pico were padded with single-beam collected in 2001 under the project GEMAS ([Quartau et al., 2003, 2002](#)). The remaining multibeam DEMs within the islands are from EMEPC and single-beam from EMODNet.

4.4. Input wind data

The surface wind data, needed as forcing input for the WW3 model, originate from ERA5 (Fifth generation of ECMWF atmospheric reanalyses of the global climate) product ([Hersbach et al., 2020](#)). ERA5 was produced as part of the implementation of the EU-funded Copernicus Climate Change Service (C3S). ERA5 provides hourly atmospheric, land, and oceanic climate variables from January 1950 to the present. The horizontal resolution of the atmosphere and wind-wave model of ERA5 is $0.25^\circ \times 0.25^\circ$ and $0.5^\circ \times 0.5^\circ$, respectively. For this study, we extracted horizontal wind components at 10 m height (U_{10} , V_{10}) with a $0.25^\circ \times 0.25^\circ$ horizontal resolution for a region covering all of the North Atlantic.

5. Wind-wave model results

5.1. General wind-wave conditions

A comparison between the time series of H_s for the buoys and the model results is shown in [Fig. 5](#) for the three long simulations, where we can see the model reproduces the main temporal pattern variations of H_s at the five buoys. For all of the buoys, scatter plots containing the intersection of model and 1h-interpolated buoy data, are shown in [Fig. 6](#) (for H_s), [Fig. 7](#) (for T_{02}) and [Fig. 8](#) (for Dir). The points on

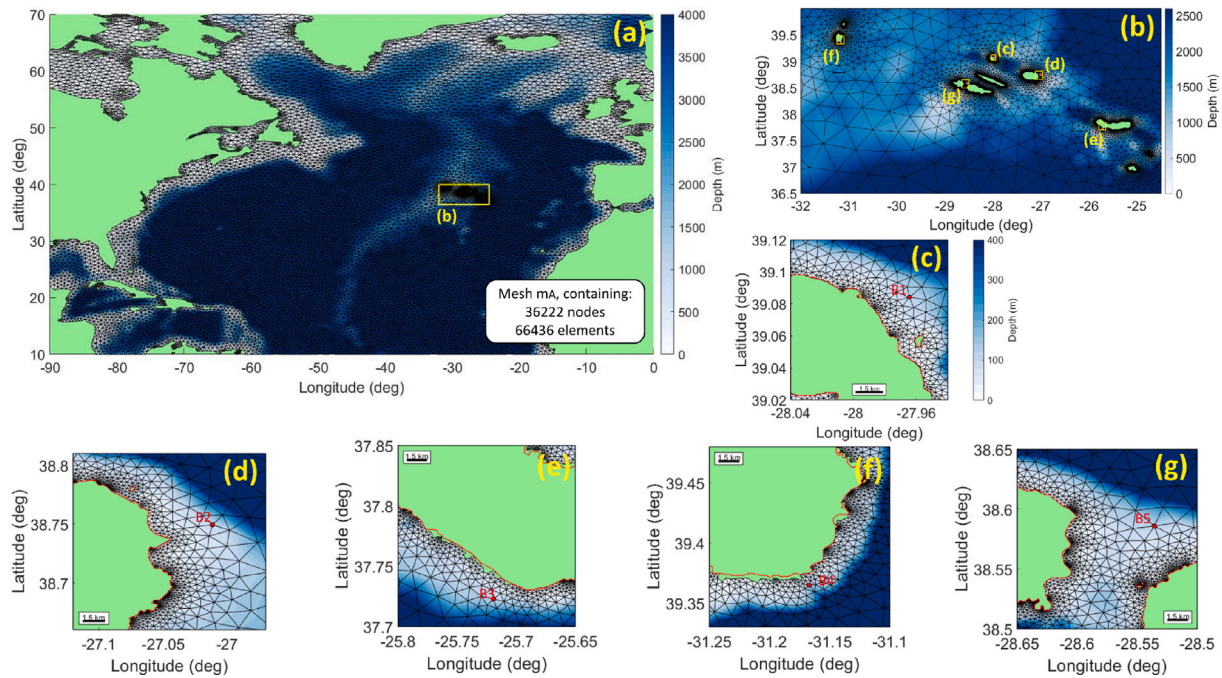


Fig. 3. Bathymetry mesh fields showing (a) the entire domain (Atlantic North), (b) the region of the Azores archipelago, and downscaled maps in the vicinity of (c) Graciosa Island (near B1), (d) Terceira Island (near B2), (e) S. Miguel Island (near B3), (f) Flores Island (near B4), (g) Pico-Faial channel (near B5). The red dots represent the in-situ measurement point locations and the red lines are the input coastlines (GSHHG). The depth colorbar in (c) is the same for the maps in (d) to (g). (For interpretation of the references to color in this figure legend, the reader is referred to the web version of this article.)

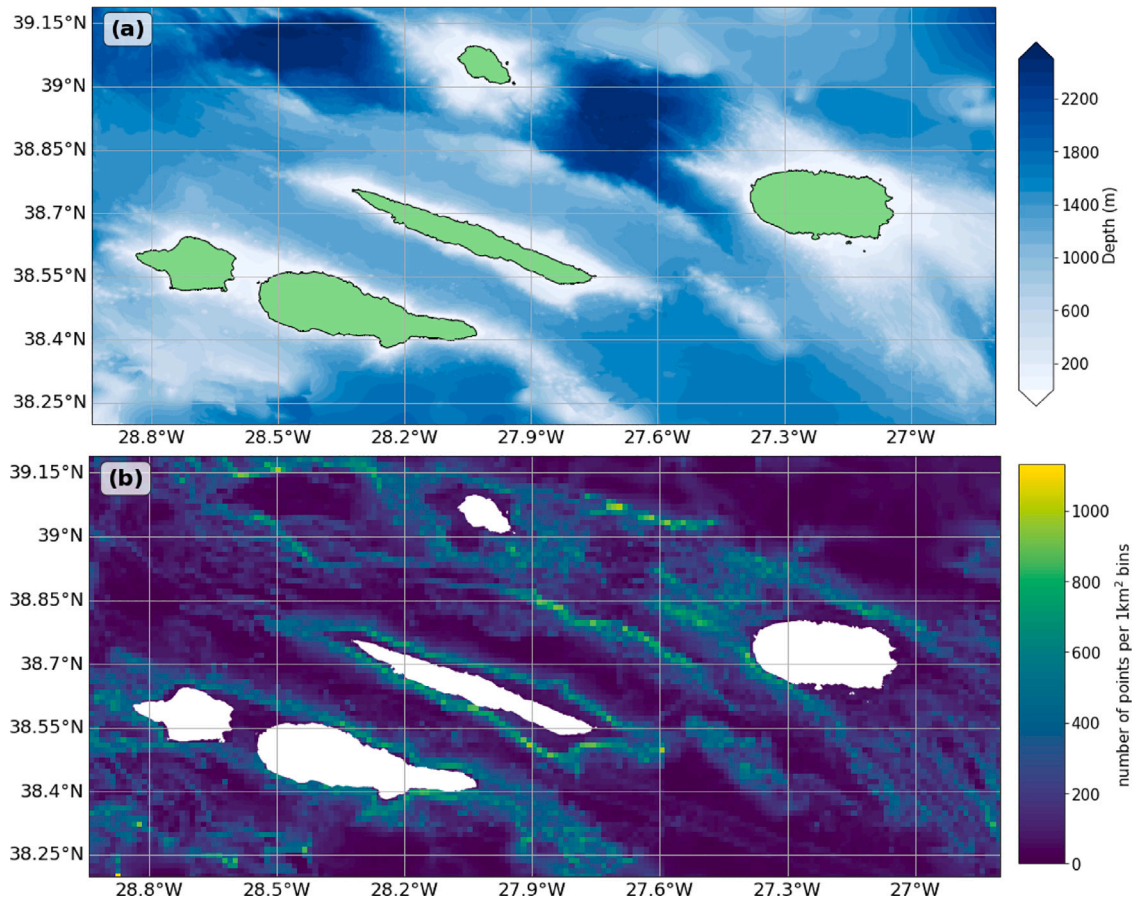


Fig. 4. Maps of the DEM_2 compiled (single and multi-beam field data) bathymetry dataset, showing the: (a) topo-bathymetric field and (b) the density map of the original isolines dataset.

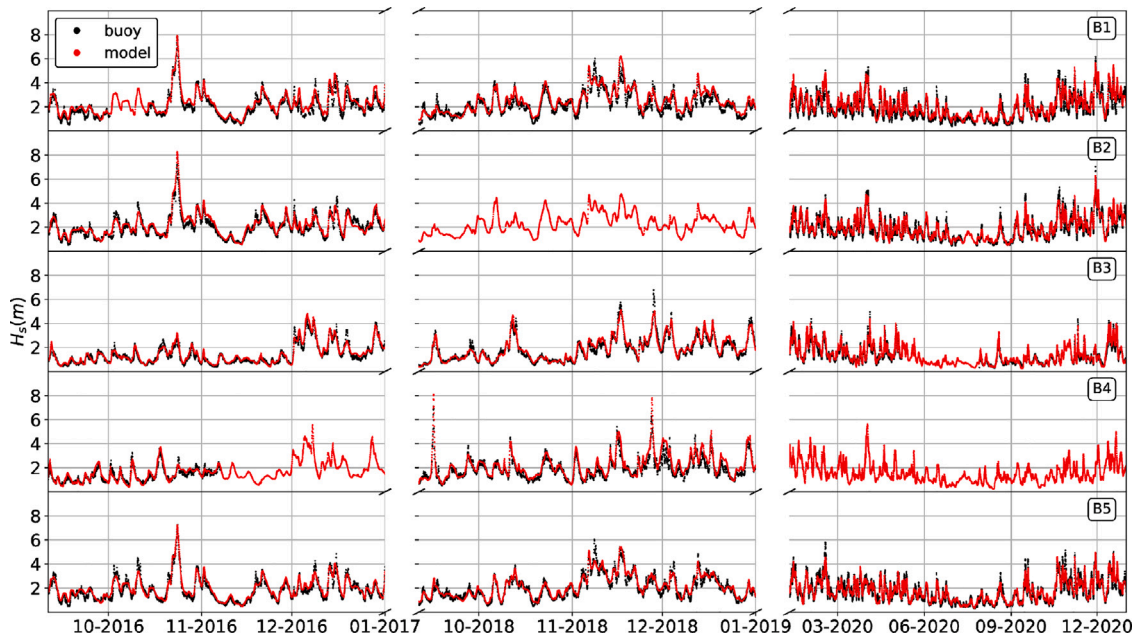


Fig. 5. Significant wave height (H_s) time series of the buoy and model datasets.

those scatter plots are color-labeled with a Kernel Density Estimator of a continuous probability density function to depict the point density (yellow are the most overposed points and dark blue the sparser ones).

The scatter plots of H_s and T_{02} both display linear regression lines between model and buoy data (red dashed lines), and identity lines (grey color). The correlation coefficient (R), the root mean squared error ($RMSE$), the Bias, and the scatter index (SI) error metrics (described in Appendix B), which are widely used in calibration and/or validation studies of the WW3 model (Adbolali et al., 2020; Oliveira et al., 2020b; Stopa et al., 2016; Rusu et al., 2008), and the number of sea states (N), as well as the model and buoy means (μ_m and μ_b) and standard deviations (σ_m and σ_b) are shown in the H_s and T_{02} scatters. Additionally, the mean, minimum, and maximum of R , $RMSE$, $Bias$ and SI , for H_s and T_{02} , are summarized in Table 5. Visualizing the scatters in Figs. 6 and 7, the model shows a good fit with the observations.

For H_s , in all buoys, the R metric was always higher than 0.95, and the mean values of $RMSE$, $Bias$ and SI (0.30 m, 0.12 m and 0.15 respectively) were relatively low. Regarding T_{02} , R was lower or equal to 0.90 in all the buoy points. In absolute values, $RMSE$ and $Bias$ for T_{02} (averaging 0.97 s and -0.71 s, respectively) were higher than for H_s . Overall, the model shows good accuracy both for H_s and T_z , although H_s has consistently better error metrics.

For the Dir scatters (Fig. 8), a high proportion of points would not be adequately compared quantitatively through the previously mentioned error metrics, as the data is periodic between $0^\circ N$ and $359^\circ N$. For instance, for Dir values from $\sim 330^\circ N$ to $\sim 30^\circ N$ (NNW to NNE) although the model was close to the measured data, the error metrics did not show that (in B1 and B5 there was a high amount of data in that Dir range). Therefore, in a case where there is a buoy observation in the $\sim 330^\circ N$ – $\sim 359^\circ N$ range and a model result in the $\sim 0^\circ N$ – $\sim 30^\circ N$ range, the absolute anomaly between would be more than 200° when that value should be around 0° – 60° . Hence, in the scatters of Dir , the error metrics were not calculated (only the buoy and model means and standard deviations). Nevertheless, two identity lines ($y = x$ and $y = 360 - x$) are shown to help visualize the model fit (especially for B1 and B5).

The maximum absolute difference between model and buoy means (μ_m and μ_b) of Dir was 25° (B1), and the minimum was 1° (B4). On the other hand, absolute differences between model and buoy standard

Table 5

Mean, minimum and maximum of the error metrics for H_s and T_{02} .

Significant wave height (H_s) [m]			
Metric	Mean	Min. [buoy (s)]	Max. [buoy (s)]
R	0.96	0.95 [B1, B4]	0.97 [B3]
$RMSE$	0.30	0.24 [B3]	0.36 [B1, B4]
SI	0.15	0.14 [B2]	0.18 [B4]
$Bias$	0.12	0.06 [B5]	0.18 [B1]
Mean wave period (T_{02}) [s]			
Metric	Mean	Min. [buoy (s)]	Max. [buoy (s)]
R	0.88	0.86 [B4]	0.90 [B2]
$RMSE$	0.97	0.84 [B1]	1.14 [B5]
SI	0.10	0.09 [B1, B2]	0.11 [B3, B5]
$Bias$	-0.71	-0.89 [B5]	-0.52 [B1]

deviations (σ_m and σ_b), ranged between 3° (B3) and 21° (B5). Although no error metrics were presented, the accuracy of the model appeared to be adequate through the scatter fits and the reduced differences between model and buoy means.

5.2. Storm events

The ability of WW3 to reproduce the six wind-wave storms introduced in Section 3.2 is studied in detail. Here the purpose is to assess the accuracy of the WW3 model when simulating different storms nearshore, as it is known that mathematical models can struggle to represent these fast and complex events. Fig. 9 displays the time series of H_s , T_m (comparison between T_{02} and T_z) and Dir for all the storms (model and wave buoy datasets). The model was generally in tune with the five in-situ measurements, although generally higher oscillations occurred near the peaks of H_s and T_z time series.

Also, the maximum values of H_s and T_z , as well as Dir means for the six storms are all listed in Table 6. The absolute maximum values of the model H_s data, the buoy H_s data and the H_s anomalies were, respectively, 10.39 (B4, S_d), 10.06 m (B3, S_d) and 3.32 m (B3, S_d). The absolute minimum values of the model H_s data, the buoy H_s data

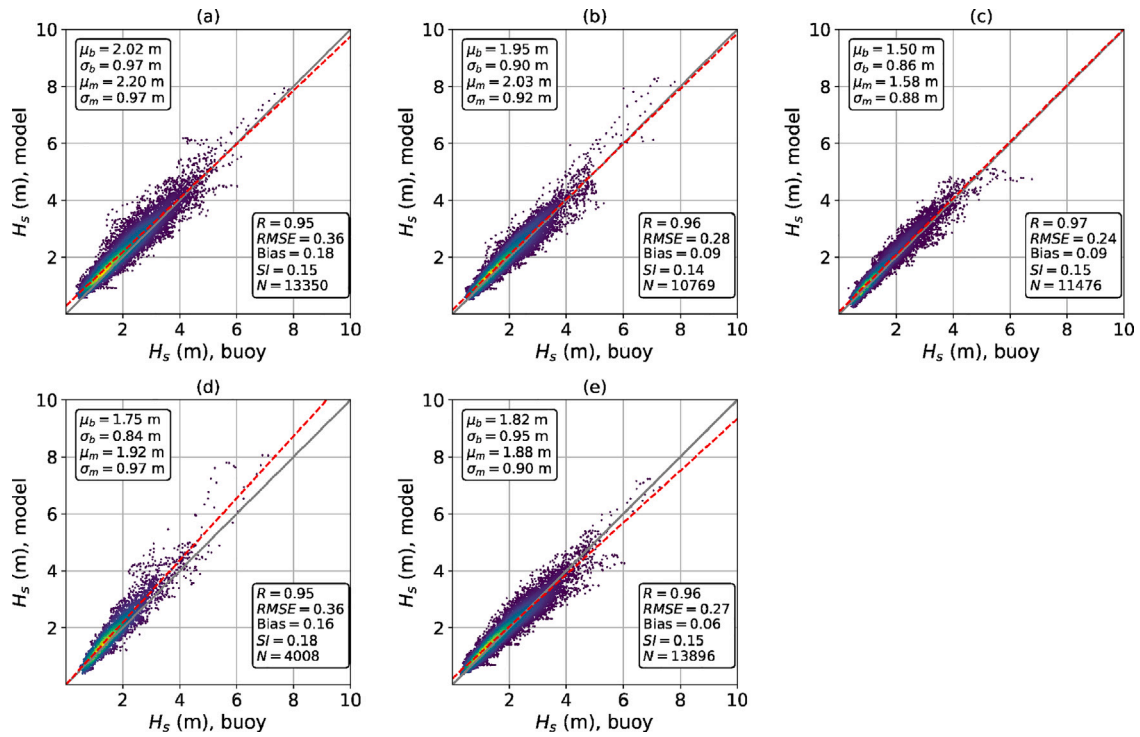


Fig. 6. Model-buoy H_s scatter plots for: (a) B1, (b) B2, (c) B3, (d) B4, (e) B5. (For interpretation of the references to color in this figure legend, the reader is referred to the web version of this article.)

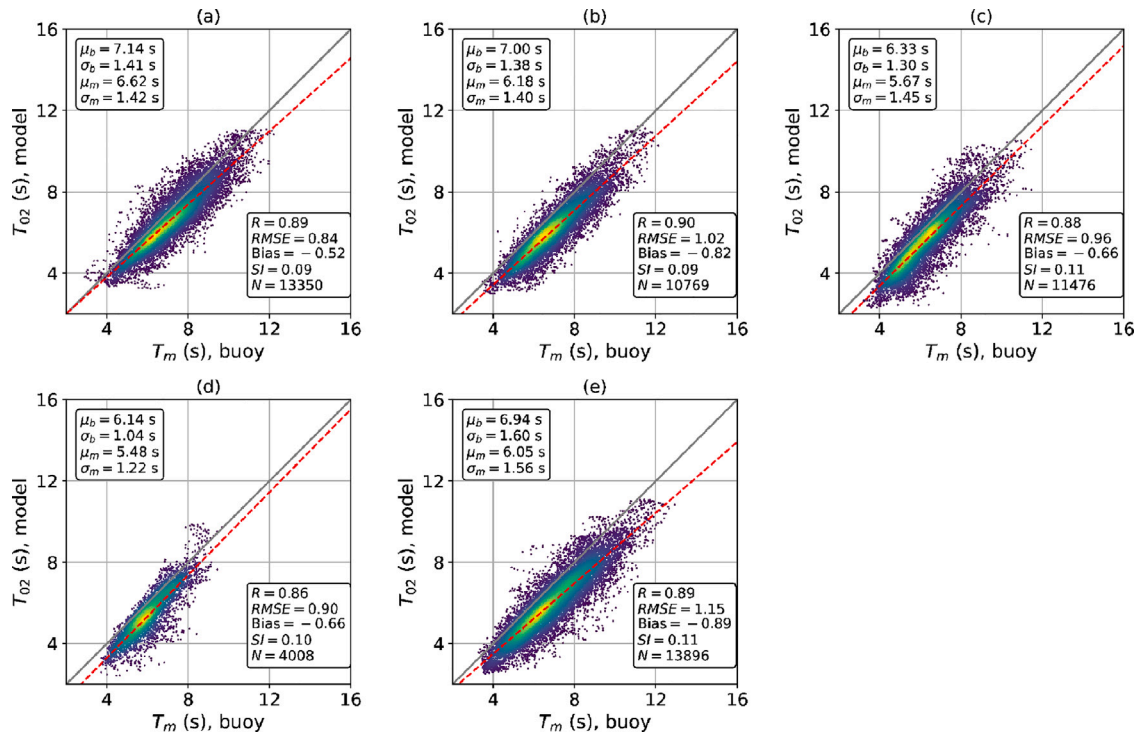


Fig. 7. Model-buoy T_{02} scatter plots for: (a) B1, (b) B2, (c) B3, (d) B4, (e) B5. (For interpretation of the references to color in this figure legend, the reader is referred to the web version of this article.)

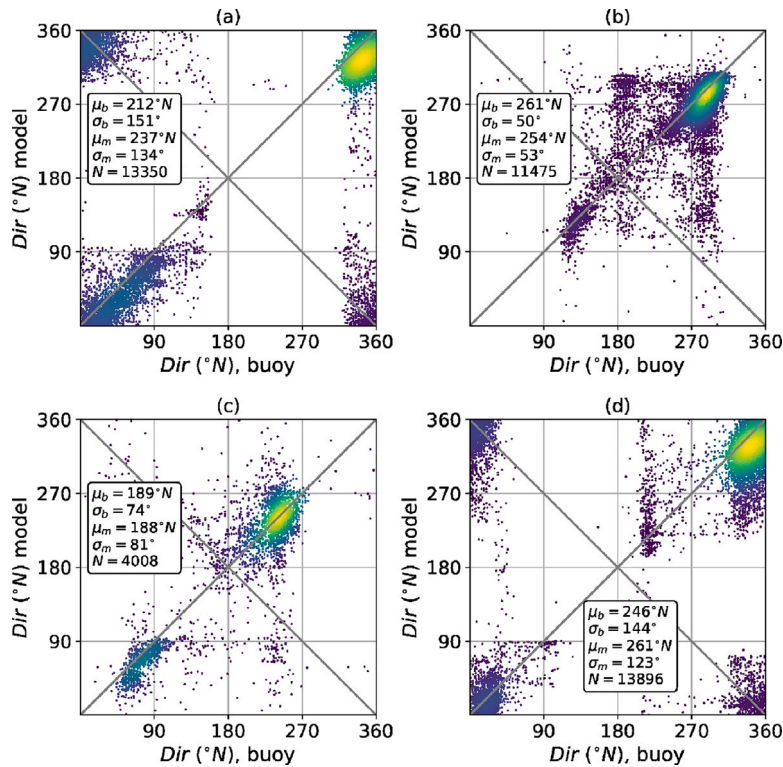


Fig. 8. Model-buoy *Dir* scatter plots for: (a) B1, (b) B3, (c) B4, (d) B5. (For interpretation of the references to color in this figure legend, the reader is referred to the web version of this article.)

and the H_s anomalies were, respectively, 2.36 m (B4, S_c and B3, S_f), 2.18 m (B4, S_d) and -0.54 m (B4, S_d) and, finally, the most accurate anomaly (the smaller anomaly in absolute value) was 0.01 m (B2, S_d). Moreover, the model always underestimated the maximums of T_z , and, in most cases overestimates the maximums of *Dir*, as seen in the anomalies of Table 6.

5.3. Performance and scalability

The performance and scalability of the model on two HPC environments (the cluster ARGUS-HPC and the supercomputer BOB-HPC) are analyzed, through multiple test simulations. Those simulations were always performed for a fixed timeframe between September 23, 2019 and October 7, 2019, which includes the passage of hurricane Lorenzo (S_d) through the Azores archipelago. Two different numerical schemes were implemented (explicit and implicit schemes), as well as two parallel CPU partition algorithms (card deck and domain decomposition). Three different model setups, varying the numerical schemes and the parallelization algorithms, were used (EXP CD, EXP DD and IMP DD, as mentioned in Section 4.1. Also, due to technical issues (model too slow to compute results or errors running WW3 subprograms), the IMP DD was not implemented in ARGUS-HPC, and the EXP DD setup was not implemented in BOB-HPC.

The number of cores for the model performance tests was varied from 32 to 96 in ARGUS-HPC and from 32 to 1000 cores in BOB-HPC (see Table 7 and Fig. 10). Also, an unstructured mesh with 36 222 nodes and 66 436 elements (mesh m_A) was used for the simulations both in ARGUS-HPC and BOB-HPC, and a bigger mesh with 84 916 nodes and 153 838 elements (mesh m_B) – with 40 m of highest resolution in the coasts of Azores and Portugal mainland – was used only for BOB-HPC simulations. Those two unstructured grids involve the same

region limits (Atlantic North). Mesh m_B has a similar implementation to m_A but contains two coastal regions of higher resolution (Portugal mainland and Azores Islands) and a slightly higher maximum resolution near the coast (40 m).

In ARGUS-HPC, for EXP DD, the model started losing scalability for simulations with more than 48 cores, and for EXP DD, the model was scalable up to 80 cores. The IMP DD setup showed the best model performance in BOB-HPC, overall. Moreover, for IMP DD the model showed scalability, throughout all the simulation tests (up to 1000 cores). For EXP CD, the model was scalable up to 500 CPU cores.

6. Discussion

Considering the mean wind-wave characterization at the five buoys, the minimum and maximum average values of H_s were 1.50 m, in B3 (south coast of S. Miguel Island), and 1.86 m, in B1 (north coast of Graciosa Island), respectively. This difference (0.36 m) is an evidence of S. Miguel Island shadow effects on the wind-wave climate from the most predominant waves coming from north. The same kind of pattern was observed for the mean values of H_{max} , with a substantial difference between the means of B1 and B3, which is 0.52 m.

For winter conditions (December–March), the means of H_s and H_{max} are, on average, 0.46 m and 0.67 m higher than the means in global conditions, respectively. Under summer conditions (June–September), the means of H_s and H_{max} were, on average, 0.57 m and 0.84 m lower than the means in global conditions, respectively. These seasonal differences are according to what is expected due to known high seasonal wind-wave variability in the region (Morales-Márquez et al., 2020; Dodet et al., 2010).

From all the in-situ measurement data, the absolute maximum values of H_s and H_{max} , both recorded in B3, occurred during the

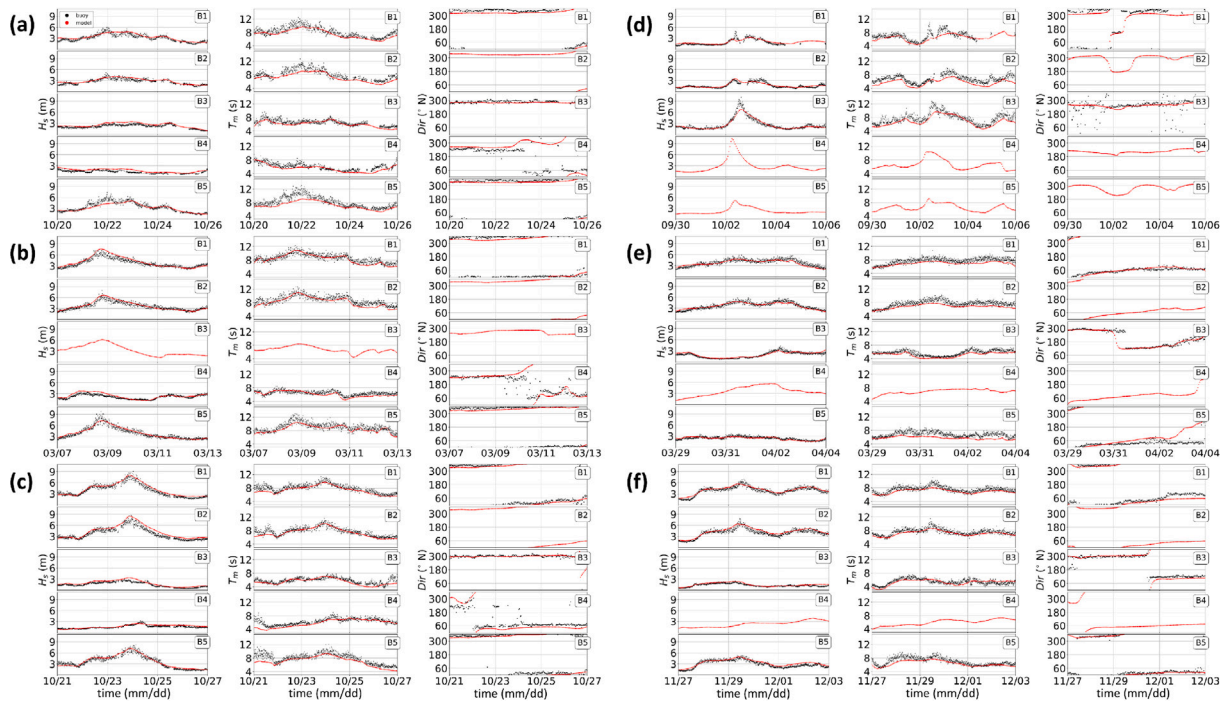


Fig. 9. Model (red dots) and buoy (black dots) wave parameter time series comparison (H_s in the left column, T_{02} in the central column and Dir in the right column) at the five buoy locations for the studied storms, from S_a , shown in (a), to S_f , shown in (f). (For interpretation of the references to color in this figure legend, the reader is referred to the web version of this article.)

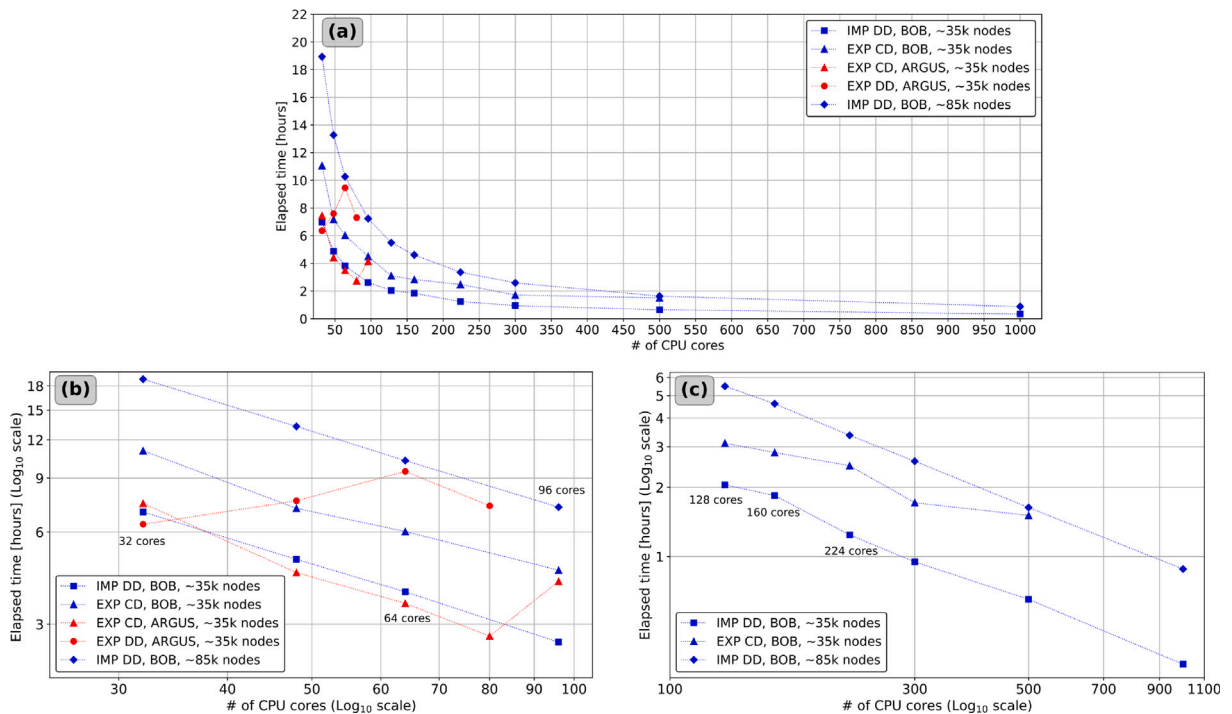


Fig. 10. Elapsed time in function of CPU cores used in WW3 performance and scalability tests displaying: (a) all simulations; (b) simulations in ARGUS and BOB for 96 or less cores (Log-Log scale plot); (c) simulations only in BOB for 128 or more cores (Log-Log scale plot). (For interpretation of the references to color in this figure legend, the reader is referred to the web version of this article.)

passage of hurricane Lorenzo (S_d), which was one of the most extreme meteorological events ever in the archipelago, in terms of damages,

precipitation and wind speed (Zelinsky, 2019). Moreover, severe wind-waves were observed in Azores during storm S_c , with absolute maximums of H_s being recorded at two of the studied buoys (B1 and B2).

Table 6

Maximum values of H_s and T_{02} , and means of \bar{Dir} for buoy and model datasets, for the six studied storms. Anomalies, corresponding to the difference between the buoy and model values, are also displayed (red anomalies are positive values and blue values are negative values).

Event (year of storm)	Buoy	max(H_s) [m] (model/buoy/ anomaly)	max(T_{02}) [s] (model/buoy/ anomaly)	\bar{Dir} [°N] (model/buoy/ anomaly)
S_a (2012)	B1	4.76/6.08/ 1.32	9.7/12.4/ 2.7	323/346/ 23
	B2	4.07/5.11/ 1.04	9.1/12.7/ 3.6	326/-/-
	B3	3.42/3.27/ -0.15	7.4/8.4/ 1.0	280/291/ 11
	B4	2.64/2.18/ -0.54	8.1/8.4/ 0.3	280/216/ -64
	B5	5.07/7.30/ 2.23	9.1/13.0/ 3.9	328/342/ 14
S_b (2013)	B1	7.61/7.36/ -0.25	10.9/12.3/ 1.4	332/214/ -118
	B2	6.60/7.91/ 1.31	10.9/12.8/1.9	336/-/-
	B3	6.11/-/-	8.4/-/-	274/-/-
	B4	3.79/3.40/ -0.39	7.3/8.2/ 0.9	269/226/ -43
	B5	7.22/9.74/ 2.52	10.3/13.0/ 2.7	334/301/ -33
S_c (2016)	B1	8.06/9.05/ 0.99	9.7/11.3/ 1.6	262/138/ -124
	B2	8.46/8.75/ 0.29	10.1/11.6/ 1.5	269/-/-
	B3	3.37/2.92/ -0.45	7.1/7.8/ 0.7	300/304/ 4
	B4	2.36/3.27/ 0.91	7.4/9.0/ 1.6	39/80/ 41
	B5	7.23/8.21/ 0.98	9.4/12.1/ 2.7	349/187/ -162
S_d (2019)	B1	3.26/4.87/ 1.61	7.8/11.0/ 3.2	263/307/ 44
	B2	3.49/3.50/ 0.01	7.4/10.1/ 2.7	241/204/ -37
	B3	6.74/10.06/ 3.32	9.7/12.7/ 3.0	243/255/ 12
	B4	10.39/-/-	10.4/-/-	216/-/-
	B5	5.16/-/-	9.1/-/-	259/-/-
S_e (2019)	B1	4.72/5.83/ 1.11	7.7/10.8/ 3.1	72/66/ -6
	B2	4.75/5.80/ 1.05	7.8/10.3/ 2.5	73/-/-
	B3	3.27/4.24/ 0.97	6.1/7.6/ 1.5	154/172/ 18
	B4	5.64/-/-	7.7/-/-	83/-/-
	B5	2.84/3.74/ 0.9	6.6/8.8/ 2.2	74/40/ -34
S_f (2020)	B1	5.68/6.98/ 1.3	8.1/11.0/ 2.9	196/134/ -56
	B2	6.37/7.88/ 1.51	8.6/11.5/ 2.9	196/-/-
	B3	2.36/2.43/ 0.07	6.1/7.5/ 1.4	305/293/ -12
	B4	3.45/-/-	7.0/-/-	45/-/-
	B5	4.94/5.32/ 0.38	7.6/9.6/ 2.0	211/173/ -38

Table 7

Elapsed times and CPU core usage for WW3 test simulations (in ARGUS-HPC and BOB-HPC) applying explicit card-deck (EXP CD), explicit domain decomposition (EXP DD) and implicit domain decomposition (IMP DD) model setups.

CPU cores	Elapsed times (seconds)				
	EXP CD (ARGUS and mesh m_A)	EXP DD (ARGUS and mesh m_A)	EXP CD (BOB and mesh m_A)	IMP DD (BOB and mesh m_A)	IMP DD (BOB and mesh m_B)
32	26816	22899	39813	25124	68148
48	15917	27329	25824	17592	47791
64	12628	34075	21692	13772	36947
80	9874	26310	-	-	-
96	14908	-	16211	9437	26056
128	-	-	11187	7382	19778
160	-	-	10194	6634	16610
224	-	-	8930	4472	12107
300	-	-	6174	3413	9342
500	-	-	5435	2346	5883
1000	-	-	-	1226	3177

The highest and lowest means of T_z were recorded in B1 and B3, respectively, similarly to what happens for the wind-wave parameters H_s and H_{max} . The variability of T_z , under global conditions, is shown to be low when compared to H_s variability. There was also some agreement between the occurrence of T_z and H_s maximum values under mean and storm conditions. For instance, absolute maximum values of T_z that were recorded at 2017/02/27, reaching values of 16.60 s (B5, at 13:40), 16.40 s (B2, at 18:00) and 15.30 s (B1, at 18:40), occurred at roughly similar times as high maximums of H_s that day (6.19 m at 16:40 for B1, 5.67 m at 21:30 for B2, and 8.33 m at 15:20 for B5). These patterns point to a high linear correlation between T_z and H_s , which (Ferreira and Guedes Soares, 2002) also observed for

some conditions. However, the authors showed that a bi-variate density function tends to present the best fit between the two variables.

The two buoys on the northeast coasts of Graciosa and Terceira Islands (B1 and B2) are exposed to the most predominant and energetic wind-waves coming from north to northwest (as shown by the wave-roses in Fig. 1b). However, for example, in B1 (where the wind-waves were overall more severe) the mean \bar{Dir} under global, winter and summer conditions are 211°N, 244°N and 189°N respectively. Nevertheless, because \bar{Dir} standard deviations are high (e.g., in B1 for global conditions is 151°), the mean \bar{Dir} is not the best indicator of the directional wind-wave patterns, because of the cyclic nature of \bar{Dir} , which leads to less intuitive results than the wave-roses. Additionally, the wave buoys B1 and B5 possess much higher \bar{Dir} standard deviations than B3 and B4, with differences of at least 79°. These standard deviation discrepancies roughly show that, on one hand, B1 and B5 display less island shadows of the most predominant wave directions. On the other hand, since B3 and B4 are highly protected from waves coming from the north (especially B3), the wind-wave climate was more stable in these two locations (in terms of H_s and T_z).

The influence of island shadow effects on the mean wind-wave conditions is highlighted by comparing the northernmost buoy (B1) to the southernmost buoy (B3), since most wind-waves come from the north. Since B1 is located north of Graciosa island, this clearly shows how S. Miguel Island affects the wind-waves predominantly from northern areas. Moreover, wave-roses help to characterize other island wave shadows. For example, the shadow effect induced by Flores Island in B4 was noticeable as most northwest waves do not arrive or lose most of their energy before reaching the buoy, in opposition to other exposed buoys (e.g., B1 and B4). Moreover, in B5 waverose, two wave shadow effects were also detected although they are not fully discernible. In that case, the directions around W and E displayed almost no wave energy (which is coherent with the position of the nearest islands to B5).

Four of the six studied storms in Azores came from northward directions, three of them associated with extratropical storms. Also, one of the two tropical origin storms, S_d , that reached Azores from southwest, generated wind-wave energy comparable to wind-waves associated with extratropical storms on the studied buoys. This fact contrasts with the west European coast where the more energetic storms are induced by winter storms of extratropical origin (Oliveira et al., 2020a).

For the three periods of long WW3 simulations, the error metrics of H_s show (Table 5) that the model represents the nearshore wind-wave climate with good accuracy, and comparable with results that previously validated WW3 (e.g., Oliveira et al., 2020b; Stopa et al., 2016). For H_s lower than 4 m, the model generally overestimates the observation data. However, the model tends to underestimate H_s for sea states with H_s above 4 m. Moreover, at B3, the model presents the best metrics, mainly because the wave climate was less severe due to S. Miguel island shadow, since the model is more accurate for mean rather than storm conditions.

The R metric of T_{02} for all buoys is equal to 0.88 on average, which is 0.08 lower than for H_s . Also, for all buoys, the Bias metric and the comparison of model and buoy means show that the model data (T_{02}) was consistently lower than the buoy data (T_z). Hence, there seems to exist a negative offset affecting the correlation. This kind of behavior for T_{02} in WW3 in relation to observed T_z was also observed and studied in Swain et al. (2017). One of the reasons for this negative offset could be that the model wind-wave parameter T_{02} is an estimate of the observed T_z . Another potential reason to that deviation could be that frequencies lower than 0.05 Hz were not modeled. In case lower spectrum frequencies are considered, it could potentially lead to higher and more accurate values of T_{02} .

The H_s Bias in the long simulations was always positive (from 0.06 to 0.18 m), indicating a general overestimation of the model for lower wave heights. Other papers also presented similar overestimations of

modeled H_s for lower waves (Li et al., 2016; Bi et al., 2015) and even for storm-induced waves (Rahimian et al., 2022; Moghimi et al., 2020). The general overestimation of the model would be due to a systematic bias in the atmospheric forcing, as discussed further in this section. The bias in the wind speed directly affects the total energy and therefore H_s , while it has less effect on T_m . Such biases are more pronounced during severe events.

Analyzing modeled Dir at the five buoy locations makes it possible to visualize the islands' shadow effects on the modeled wind-wave climate. For instance, in B3, there was an absence of data between 300°N and 90°N, and generally the wave direction is well reproduced by the model. Also, in B5, the western and eastern wave directions are well covered by the model, due to Faial and Pico island shadows. Although error metrics were not performed for Dir , the Dir mean conditions are generally well represented by the model. Overall, under mean conditions, the model represented the main wind-wave spatial and temporal variation patterns in the Azores Archipelago.

Regarding the model results under storm conditions, the average of the anomalies of the H_s maximum values (subtraction of buoy by model maximums), accounting for all storms and all buoys, was 0.79 m. This shows how WW3 underestimates the model in storm scenarios. In total, there were 20 positive anomalies and five negative anomalies ($\max(H_{s,b}) < \max(H_{s,m})$). However, if we account for anomalies where the maximums of $H_{s,m}$ are higher than 5 m, there is only one negative anomaly. This is an exceptional case, where $\max H_{s,m}$ (7.61 m) was higher than $\max(H_{s,b})$ (7.36 m), and happened in event S_b for B1. However, this anomaly (−0.25 m) was much lower than the set of all anomalies for B1 (1.1 m). Additionally, in the time series plots, the model data shows good fit to the measured wind-wave patterns. However, it is important to note that for S_a in B5 and S_d in B3 the model underestimation, both in H_s and T_{02} , is more visible throughout most of the storm activity in those points.

Model H_s underestimation during storm events could be partly due to coarse ERA5 atmospheric forcing resolution (around 27 km space, and 1 h in time), leading to inaccurate spatio-temporal wind variations representation (Cavaleri et al., 2020). For instance, the surface wind field gradient is more variable under tropical storm conditions at shorter distances. These are known causes for underestimation in other WW3 hindcast studies using reanalysis winds from ECMWF products, like ERA Interim (deprecated) or ERA5 (e.g., Kodaira et al., 2022; Waseda et al., 2021; Cavaleri et al., 2020; Stopa, 2018; Campos and Soares, 2016; Cavaleri, 2009; Rusu et al., 2008). Hence, finer spatial and temporal resolution of forcing should be considered. The input ERA5 winds were not validated in this study for the Azores region due to a lack of access to local meteorological observations. As a result, ERA5 wind fields can present some errors representing local wind patterns during the analyzed storms. The reasons for the discrepancies between model results and data could also be caused by missing in the model of current effects on waves (Bakhtyar et al., 2020; Moghimi et al., 2020; Cavaleri et al., 2007), wave diffraction (Stopa et al., 2013), swells from the open boundary (Cavaleri et al., 2007), or unsatisfied physics in the source terms (Cavaleri et al., 2020).

The WW3 model has different wave input-dissipation source term packages such as ST1 (Komen et al., 1984), ST2 (Tolman and Chalikov, 1996), ST3 (Bidlot et al., 2007; Janssen, 1991), ST4 (Ardhuin et al., 2010) and ST6 (Zieger et al., 2015; Rogers et al., 2012). In our work, the input-dissipation source term ST4 was used, as it has been applied in most of the current wind-wave forecast systems (e.g., Campos et al., 2022a; Oliveira et al., 2020b; Saulter et al., 2016). However, using different source term packages could improve our model results for some specific wave conditions.

The source terms ST4 and ST6 have been considered the best performing input-dissipation source terms (e.g., Soran et al., 2022; Kalourazi et al., 2021; Umesh and Behera, 2020; Beyramzadeh et al., 2021). Although ST6 is the most recent addition to WW3, it has been shown that it does not always give the best results. For instance, under

extreme wave conditions, it was shown that ST6 and ST4 terms had similar performances (e.g., Kalourazi et al., 2021) or that ST6 performs better (Soran et al., 2022). However, ST4 was recommended over ST6 when considering year-round wind-wave climate studies (Soran et al., 2022) or for open sea conditions (e.g., Bi et al., 2015), although ST4 and ST6 can also show comparable results at open sea (Foli et al., 2022). On the other hand, ST6 outperformed ST4 when depicting swell energy variations (Bi et al., 2015) or at higher resolution subgrids in nearshore regions (Foli et al., 2022). Also, the recent stabilization parameter to the input-dissipation source terms STAB2 (WW3DG, 2019) is worth mentioning, which could improve model accuracy for some wave conditions (Foli et al., 2022). This should also include testing new versions of ST4, as this source term package is still under development (Romero, 2019).

Although phase averaged wave models like WW3, SWAN (Booij et al., 1999), and MIKE21SW (DHI, 2017) can accurately simulate generation, dissipation, nonlinear wave interactions, and refraction phenomena in deep and shallow water, they cannot simulate wave diffraction. Wave diffraction is a higher-order phenomenon, which occurs if the spatial scales of certain bathymetric features are in proportion to the wavelength. It leads to strong non-linear effects, which tend to significantly change the direction of the wave action propagation. Several studies have been done to approximate these phenomena in phase averaged spectral wave models (e.g., Holthuijsen, 2007; Liao et al., 2011), which is not straightforward since the physics of wave diffraction are strongly linked to the phases of certain spectral wave components. Therefore, phase resolving models are actually the ones that are predestined to be used for this kind of problem.

Nevertheless, due to the slowness of phase resolving models and the absence of the ability to model wind-wave growth, a considerable amount of work was done to have a reliable approximation of diffraction in phase averaged models. SWAN and MIKE21SW models can account for some diffraction effects by including the additional term derived from the mild-slope equation (Holthuijsen, 2007). It is expected then that phase averaged models with wave diffraction parameterizations could improve wave predictions in island environments for some specific wave conditions (e.g., Violante-Carvalho et al., 2021; Sartini et al., 2015; Stopa et al., 2013).

Some studies dealing with island shadow effects have been performed with MIKE21SW (e.g., Nguyen and Zhang, 2022; Jinoj et al., 2021; Eissa and Lebleb, 2015) and SWAN (Afzal and Kumar, 2022; Wu et al., 2021; Violante-Carvalho et al., 2021; Gonçalves and Guedes Soares, 2020; Björkqvist et al., 2020; Yang et al., 2020; Canals Silander and García Moreno, 2019; Sandhya et al., 2014; Stopa et al., 2013). Some of these modeling studies considered wave diffraction (Afzal and Kumar, 2022; Violante-Carvalho et al., 2021; Gonçalves and Guedes Soares, 2020). In some of the studies, more than one wave model (Gonçalves and Guedes Soares, 2020; Canals Silander and García Moreno, 2019; Sandhya et al., 2014; Stopa et al., 2013), multigrid schemes (Sandhya et al., 2014) or low-resolution single grids (Yang et al., 2020) were used.

Mesh resolutions of around 55 km have successfully simulated wave climate in deepwater regions (e.g., Brus et al., 2021; Oliveira et al., 2020a; Stopa et al., 2016). However, it is expected that higher-resolution discretizations could improve model performance under extreme atmospheric events in deep waters.

At ARGUS-HPC, the model was scalable up to 96 cores (maximum number of cores available to us) for the EXP CD model setup. However, in this HPC for the EXP DD setup, the model was only scalable for up to 48 cores. For BOB-HPC, the model was scalable up to 1000 cores (maximum number of cores used) for the IMP DD setup and 500 cores for the EXP CD setup. Furthermore, in ARGUS-HPC, the EXP DD performance was the best for the lowest cores (32) and the EXP CD, also performances from 48 to 80 cores are better than the performances for the IMP DD (in BOB-HPC) for the same number of cores. Besides that, EXP CD and IMP DD performance comparisons are inconclusive,

as the two model setups were simulated in different HPC environments with different hardware and Fortran compilers. These differences could justify the better performance of EXP CD in ARGUS-HPC than IMP DD in BOB-HPC for a lower number of cores.

7. Conclusions

This study characterized the nearshore wind-wave climate of the Azores archipelago based on 12 years of in-situ measurements at five nearshore locations. The characterization was based on the analysis of significant wave height (H_s), mean wave zero-crossing period (T_z) and mean wave direction (Dir) parameters under mean and storm conditions. The ability to simulate local wave conditions by an unstructured WW3 model covering the north Atlantic with high resolution around the Azores Archipelago was analyzed. A mesh of resolutions ranging from 55 km offshore to around 50 m nearshore the Azores islands was utilized. Finally, the computational performance and scalability of the unstructured WW3 model were studied for different model setups in two HPC environments.

Although there is a significant lack of data in the 12 years of measurements at the five buoys, those datasets presented a typical seasonal variability of wave climate in the North Atlantic. Moreover, the datasets presented the main island shadow impacts in the mean wave conditions at the buoys, which is most evident at B3. For instance, H_s and H_{max} mean values were higher at B1 and B2 (both in the north of the Archipelago) than at B3 (in the South), which clearly shows how S. Miguel Island affects wind-waves coming predominantly from the north.

For the six recorded storm events analyzed, H_s was in general higher on the north coasts of the archipelago. However, these differences depend on the storm track. For storm S_c , H_s differences up to approximately 7 m were observed between the north and south of the archipelago. However, for tropical related storms S_a and S_d , H_s was higher on the buoys located on the south coast of the archipelago. Under hurricane Lorenzo (S_d), the island shadow effect caused by Graciosa, Pico, and Faial to waves coming from SW to S, led to differences in the maximum of H_s of up to approximately 6.5 m between the archipelago's south (B3) and north (B1 and B2) buoys.

The unstructured WW3 model was validated for nearshore mean wind-wave conditions in the Azores, for three different periods covering about one year and eight months. In general, the model represented the main nearshore wave climate features with good accuracy, as shown by the R, RMSE, Bias, and SI statistical metrics for the wind-wave parameters H_s and T_{02} . The H_s parameter has demonstrated the best fit to the observations, presenting the best error metrics overall. For T_{02} , since this variable is compared with T_z from the buoys (which are not precisely the same wave parameter), the metrics R and Bias showed a lower model performance. Qualitatively, modeled Dir showed good accuracy with means and standard deviations reasonably close to the in-situ measurements. Overall, the model reproduced the main island shadow effects on the wind-wave nearshore climate of the archipelago.

Model results highlight the challenges of modeling wind-waves around islands under storm conditions. In most cases, the model underestimated H_s recorded by the nearshore buoys during storms (the difference between buoy and model H_s maximum values is, on average, 0.79 m). The highest model underestimation (3.3 m) occurred during hurricane Lorenzo (S_d), the most severe wind-wave storm recorded. In this case, buoy B3 recorded a maximum H_s of 10.06 m, and for that location, the maximum H_s given by the model was 6.74 m. One of the few exceptions to the underestimation trend occurred during S_b in B1, where the model overestimated the maximum of H_s by 0.25 m. However, the model showed an overall good fit throughout the S_b storm.

The model's computational performance and scalability were studied in two HPC environments. For the supercomputer BOB-HPC, with

the implicit domain decomposition model implementation, WW3 had the best overall performance. With the implicit domain decomposition, the model was scalable for up to 1000 cores. With the explicit card-deck setup the model was scalable up to 500 cores. Unfortunately, the explicit domain decomposition setup was not implemented in BOB due to technical errors that were not solved. Furthermore, for the HPC cluster ARGUS-HPC, the two functional model setups were the explicit card-deck (scalable up to 80 cores) and the explicit domain decomposition (scalable up to 32 cores). The efficiency of the model for these two implementations is inconclusive.

The meshing methodology used in this work relies on open-source software OM2D, for Matlab (Roberts et al., 2019). This methodology has shown to be fast and effective in creating automatically optimized unstructured meshes. Moreover, with OM2D, it is easy to set up various unstructured mesh parameters (e.g., mesh grade, minimum and maximum resolutions, fixed points), boundary boxes, and inserting bathymetry and coastline inputs to, for example, increase mesh resolution in specific areas of interest. Future studies applying the WW3 unstructured model, especially for high-resolution nearshore modeling, could apply the same meshing methodology presented in this work.

Future work should consider higher resolution atmospheric inputs and add the effect of local currents on the surface waves. Moreover, a comparison of the model results with satellite wind-wave data around the islands, and more global in the Atlantic North, could be studied in detail. Coupling the model with a storm surge model and adding boundary conditions to this domain (to take more swell information into account) could help the accuracy under these circumstances. Moreover, the 55 km model resolution in deep water regions could be refined to around 10 km to simulate storm events, as wind-wave models like WW3 require higher resolution than conventional storm surge models to provide accurate results. These results would facilitate further WW3 calibrations and understanding physics source-term options (e.g. depth-induced breaking, bottom friction) that affect the representation of local nearshore processes.

Overall, this paper characterized mean and storm wind-wave conditions, highlighting the island shadow effects in the Azores, which could be further studied with more field measurements.

CRediT authorship contribution statement

Nuno M.R. Monteiro: Data-analysis, Numerical computation, Writing – original draft. **Tiago C.A. Oliveira:** Data-analysis, Numerical computation, Writing – original draft. **Paulo A. Silva:** Data-analysis, Writing – review & editing. **Ali Adbolali:** Numerical simulations, Writing – review & editing.

Declaration of competing interest

The authors declare that they have no known competing financial interests or personal relationships that could have appeared to influence the work reported in this paper.

Data availability

Data will be made available on request.

Acknowledgments

Thanks are due FCT/MCTES for the financial support to CESAM, Portugal (UIDP/50017/2020+UIDB/50017/2020+ LA/P/0094/2020), through national funds. Thanks are also due to FCT I. P. for the access to the National Network for Advanced Computing under the project CPCA/A0/7420/2020 (P.I. Tiago Oliveira). Luís Carvalheiro is acknowledged for his help with WW3 at ARGUS-HPC at the University of Aveiro. Thanks are due to Rui Quartau (Hydrographic Institute of Portugal) for making bathymetric multi-beam data available.

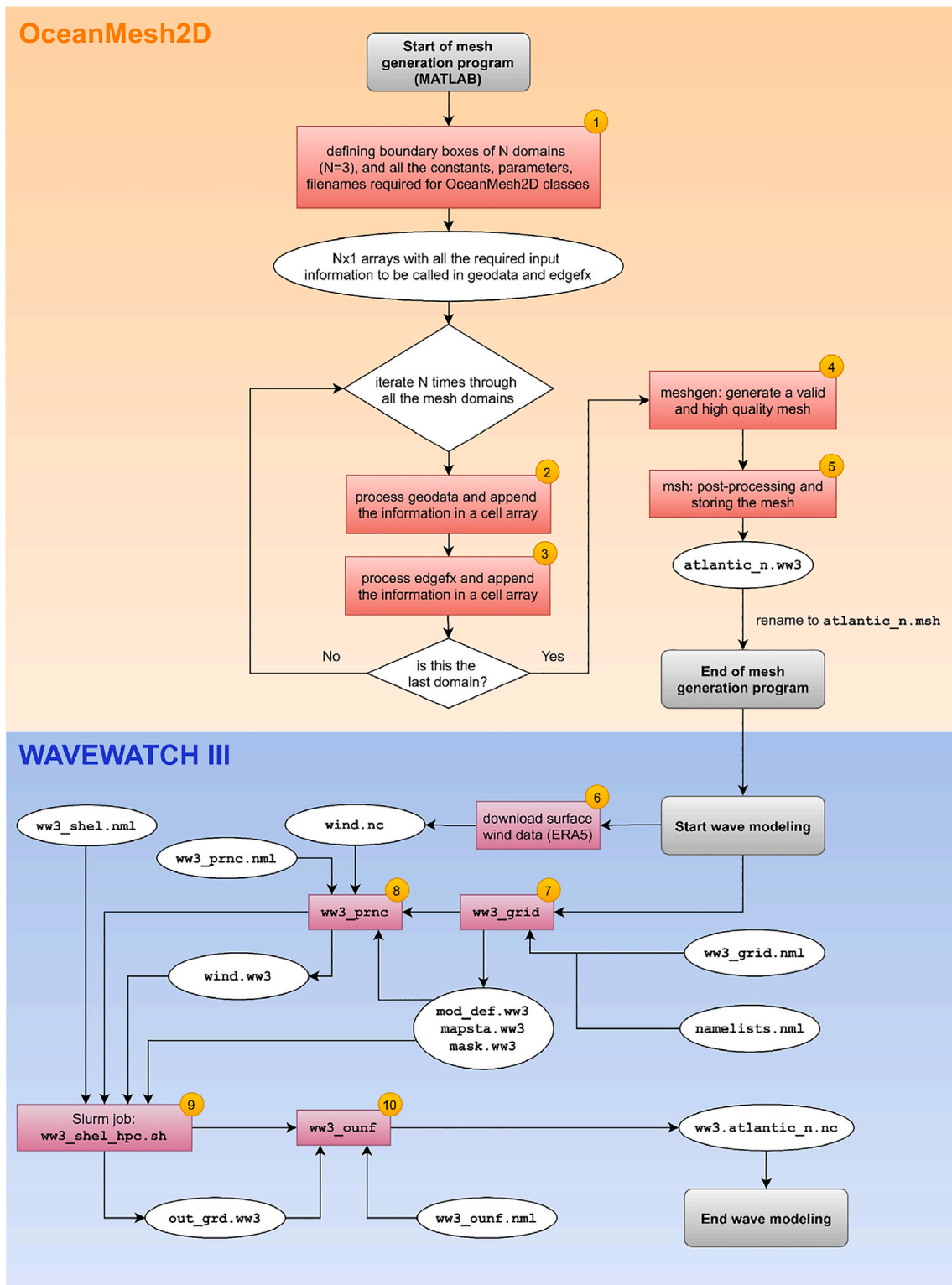


Fig. A.1. Global flowchart of the methodology for the unstructured mesh generation with OM2D and the wind-wave simulation with WW3.

Appendix A. Flowchart of the overall methodology

See Fig. A.1.

Appendix B. Error metrics

Statistical error metrics were computed to assess the WW3 model's accuracy for model datasets of five mesh nodes with the coordinates

as the wave buoys. These error metrics are the Correlation Coefficient (R), the Root Mean Square Error ($RMSE$), the Scatter Index (SI) and the Bias:

$$R = \frac{\sum_{i=1}^n (x_{m,i} - \bar{x}_m) - (x_{b,i} - \bar{x}_b)}{\sqrt{\sum_{i=1}^n (x_{m,i} - \bar{x}_m)^2 \sum_{i=1}^n (x_{b,i} - \bar{x}_b)^2}} \quad (3)$$

$$\text{RMSE} = \sqrt{\frac{1}{n} \sum_{i=1}^n (x_{m,i} - x_{b,i})^2} \quad (4)$$

$$\text{SI} = \frac{1}{x_b} \sqrt{\frac{1}{n} \sum_{i=1}^n [(x_{m,i} - \bar{x}_m) - (x_{b,i} - \bar{x}_b)]^2} \quad (5)$$

$$\text{Bias} = \frac{\sum_{i=1}^n (x_{m,i} - x_{b,i})}{n} \quad (6)$$

where x_m represents data from the wave model and x_b are the observations (buoy data).

References

- Adbolali, A., Roland, A., van der Westhuysen, A., Meixner, J., Chawla, A., Hesser, T.J., Smith, J.M., Sikiric, M.D., 2020. Large-scale hurricane modeling using domain decomposition parallelization and implicit scheme implemented in WAVEWATCH III wave model. *Coast. Eng.* 157, 103656. <http://dx.doi.org/10.1016/j.coastaleng.2020.103656>.
- Adbolali, A., van der Westhuysen, A., Ma, Z., Mehra, A., Roland, A., Moghimi, S., 2021. Evaluating the accuracy and uncertainty of atmospheric and wave model hindcasts during severe events using model ensembles. *Ocean Dyn.* 71 (2), 217–235.
- Afzal, M.S., Kumar, L., 2022. Propagation of waves over a rugged topography. *J. Ocean Eng. Sci.* 7 (1), 14–28. <http://dx.doi.org/10.1016/j.joes.2021.04.004>.
- Andrade, C., Trigo, R., Freitas, M., Gallego, M., Borges, P., Ramos, A., 2008. Comparing historic records of storm frequency and the North Atlantic Oscillation (NAO) chronology for the Azores region. *Holocene* 18 (5), 745–754. <http://dx.doi.org/10.1177/0959683608091794>.
- Andrefouet, S., Ardhuin, F., Queffelec, P., Le Gendre, R., 2012. Island shadow effects and the wave climate of the Western Tuamotu Archipelago (French Polynesia) inferred from altimetry and numerical model data. *Mar. Pollut. Bull.* 65, 415–424. <http://dx.doi.org/10.1016/j.marpolbul.2012.05.042>.
- Ardhuin, F., Rogers, E., Babanin, A.V., Filipot, J.-F., Magne, R., Roland, A., van der Westhuysen, A., Queffelec, P., Lefevre, J.-M., Aouf, L., Collard, F., 2010. Semiempirical dissipation source functions for ocean waves. Part I: Definition, calibration, and validation. *J. Phys. Oceanogr.* 40 (9), 1917–1941. <http://dx.doi.org/10.1175/2010JPO4324.1>.
- Avila, L., 2013. Tropical Cyclone Report: Hurricane Rafael (AL172012). National Hurricane Center, Miami, FL.
- Azevedo, E., Gonçalves, V., 2005. O projecto CLIMAAT e o seu contributo para a monitorização e caracterização da agitação marítima no arquipélago dos açores-4^{as} jornadas portuguesas de engenharia costeira e portuária. *Angra Heroísmo* 20.
- Bakhtyar, R., Maitaria, K., Velissariou, P., Trimble, B., Mashriqui, H., Moghimi, S., Adbolali, A., Van der Westhuysen, A.J., Ma, Z., Clark, E.P., Flowers, T., 2020. A new 1D/2D coupled modeling approach for a riverine-estuarine system under storm events: Application to Delaware river basin. *J. Geophys. Res. Oceans* 125 (9), <http://dx.doi.org/10.1029/2019JC015822>, e2019JC015822.
- Bank, R.E., 1998. PLTMG: A Software Package for Solving Elliptic Partial Differential Equations. ISBN: 978-0-89871-409-8, <http://dx.doi.org/10.1137/1.9780898719635.fm>.
- Battjes, J.A., Janssen, J., 1978. Energy loss and set-up due to breaking of random waves. In: ICCE78. ASCE, pp. 569–587.
- Beyramzadeh, M., Siadatmousavi, S.M., Derkani, M.H., 2021. Calibration and skill assessment of two input and dissipation parameterizations in WAVEWATCH-III model forced with ERA5 winds with application to Persian Gulf and Gulf of Oman. *Ocean Eng.* 219, 108445. <http://dx.doi.org/10.1016/j.oceaneng.2020.108445>.
- Bi, F., Song, J., Wu, K., Xu, Y., 2015. Evaluation of the simulation capability of the Wavewatch III model for Pacific Ocean wave. *Acta Oceanol. Sin.* 34 (9), 43–57. <http://dx.doi.org/10.1007/s13131-015-0737-1>.
- Bidlot, J., Janssen, P., Abdalla, S., Hersbach, H., 2007. A revised formulation of ocean wave dissipation and its model impact ECMWF. In: ECMWF Technical Memoranda.
- Björkqvist, J.-V., Vähä-Piikkiö, O., Alari, V., Kuznetsova, A., Tuomi, L., 2020. WAM, SWAN and WAVEWATCH III in the Finnish archipelago – the effect of spectral performance on bulk wave parameters. *J. Oper. Oceanogr.* 13 (1), 55–70. <http://dx.doi.org/10.1080/1755876X.2019.1633236>.
- Boccotti, P., 2000. Wave Mechanics for Ocean Engineering. Elsevier.
- Booij, N., Ris, R.C., Holthuijsen, L.H., 1999. A third-generation wave model for coastal regions: 1. Model description and validation. *J. Geophys. Res. Oceans* 104 (C4), 7649–7666. <http://dx.doi.org/10.1029/98JC02622>.
- Brus, S.R., Wolfram, P.J., Van Roekel, L.P., Meixner, J.D., 2021. Unstructured global to coastal wave modeling for the energy exascale earth system model using WAVEWATCH III version 6.07. *Geosci. Model Dev.* 14 (5), 2917–2938.
- Campos, R., Bernardino, M., Gonçalves, M., Guedes Soares, C., 2022a. Assessment of meteocean forecasts for Hurricane Lorenzo in the Azores Archipelago. *Ocean Eng.* 243, 110292. <http://dx.doi.org/10.1016/j.oceaneng.2021.110292>.
- Campos, R., D'Agostini, A., França, B., Damião, A., Guedes Soares, C., 2022b. Implementation of a multi-grid operational wave forecast in the South Atlantic Ocean. *Ocean Eng.* 243, 110173. <http://dx.doi.org/10.1016/j.oceaneng.2021.110173>.
- Campos, R.M., Soares, C.G., 2016. Comparison and assessment of three wave hindcasts in the North Atlantic Ocean. *J. Oper. Oceanogr.* 9 (1), 26–44. <http://dx.doi.org/10.1080/1755876X.2016.1200249>.
- Canals Silander, M.F., García Moreno, C.G., 2019. On the spatial distribution of the wave energy resource in Puerto Rico and the United States Virgin Islands. *Renew. Energy* 136, 442–451. <http://dx.doi.org/10.1016/j.renene.2018.12.120>.
- Casas-Prat, M., Wang, X.L., 2020. Projections of extreme ocean waves in the arctic and potential implications for coastal inundation and erosion. *J. Geophys. Res. Oceans* 125 (8), <http://dx.doi.org/10.1029/2019JC015745>.
- Cavaleri, L., 2009. Wave modeling—Missing the peaks. *J. Phys. Oceanogr.* 39 (11), 2757–2778. <http://dx.doi.org/10.1175/2009JPO4067.1>.
- Cavaleri, L., Alves, J.-H., Ardhuin, F., Babanin, A., Banner, M., Belibassakis, K., Benoit, M., Donelan, M., Groeneweg, J., Herbers, T., Hwang, P., Janssen, P., Janssen, T., Lavrenov, I., Magne, R., Monbaliu, J., Onorato, M., Polnikov, V., Resio, D., Rogers, W., Sheremet, A., McKee Smith, J., Tolman, H., van Vledder, G., Wolf, J., Young, I., 2007. Wave modelling – The state of the art. *Prog. Oceanogr.* 75 (4), 603–674. <http://dx.doi.org/10.1016/j.pocan.2007.05.005>.
- Cavaleri, L., Barbariol, F., Benetazzo, A., 2020. Wind-wave modeling: Where we are, where to go. *J. Mar. Sci. Eng.* 8 (260), <http://dx.doi.org/10.3390/jmse8040260>.
- Chawla, A., Tolman, H.L., Gerald, V., Spindler, D., Spindler, T., Alves, J.-H.G., Cao, D., Hanson, J.L., Devaliere, E.-M., 2013. A multigrid wave forecasting model: A new paradigm in operational wave forecasting. *Weather Forecast.* 28 (4), 1057–1078.
- Connell, J., 2015. Vulnerable Islands: Climate change, tectonic change, and changing livelihoods in the Western Pacific. 27, 1–36. <http://dx.doi.org/10.1353/cp.2015.0014>.
- DHI, M., 2017. MIKE 21 Spectral Waves FM, Spectral Wave Module User Guide. DHI Water Environment Health, Hørsholm, Denmark.
- Dodet, G., Bertin, X., Taborda, R., 2010. Wave climate variability in the North-East Atlantic Ocean over the last six decades. *Ocean Model.* 31 (3), 120–131. <http://dx.doi.org/10.1016/j.ocemod.2009.10.010>.
- Eissa, S.S., Lebleb, A.A., 2015. Numerical modeling of nearshore wave conditions at Al Huwaisat Island, KSA. *Aquat. Procedia* 4, 79–86. <http://dx.doi.org/10.1016/J.AQPRO.2015.02.012>.
- Enríquez, A.R., Marcos, M., Álvarez-Ellacuría, A., Orfila, A., Gomis, D., 2017. Changes in beach shoreline due to sea level rise and waves under climate change scenarios: application to the Balearic Islands (western Mediterranean). *Nat. Hazards Earth Syst. Sci.* 17 (7), 1075–1089. <http://dx.doi.org/10.5194/nhess-17-1075-2017>.
- Esteves, R., Valente, A.S., Reis, F.V., Azevedo, E.B., 2009. Dados Direcionais de Agitação Marítima nos Açores (Projeto CLIMAAT-Clima e Meteorologia dos Arquipélagos Atânticos). <https://onpetro.org/ISOPEIOPEC/proceedings-pdf/ISOPE19/All-ISOPE19/ISOPE-I-19-227/1128279/iso-pe-i-19-227.pdf>. ISOPE-I-19-227.
- Ferreira, J., Guedes Soares, C., 2002. Modelling bivariate distributions of significant wave height and mean wave period. *Appl. Ocean Res.* 24 (1), 31–45. [http://dx.doi.org/10.1016/S0141-1187\(02\)00066-8](http://dx.doi.org/10.1016/S0141-1187(02)00066-8).
- Foli, B.A.K., Ansong, J.K., Addo, K.A., Wiafe, G., 2022. A WAVEWATCH III® model approach to investigating ocean wave source terms for West Africa: Input-dissipation source terms. *Remote Sens. Earth Syst. Sci.* 5 (1), 95–117. <http://dx.doi.org/10.1007/s41976-021-00065-y>.
- Fortes, C., Reis, M., Pinheiro, L., Poseiro, P., Serrazina, V., Mendonça, A., Smithers, N., Santos, M., Barateiro, J., Azevedo, E., Salvador, M., Reis, F., 2020. The HIDRALERTA system: Application to the ports of Madalena do Pico and S. Roque do pico, azores. *Aquat. Ecosyst. Health Manag.* 23 (4), 398–406. <http://dx.doi.org/10.1080/14634988.2020.1807295>.
- Gonçalves, M., Guedes Soares, C., 2020. Assessment of the Wave Energy Resource in the Azores Coastal Area. pp. 26–33. <http://dx.doi.org/10.1201/9781003134572-04>.
- Gonçalves, M., Martinho, P., Guedes Soares, C., 2020. Wave energy assessment based on a 33-year hindcast for the Canary Islands. *Renew. Energy* 152, 259–269. <http://dx.doi.org/10.1016/j.renene.2020.01.011>.
- Gonçalves, M., Soares, C.G., 2020. Assessment of the wave energy resource in the azores coastal area. In: *Developments in Renewable Energies Offshore* (1st Edition). pp. 26–33. <http://dx.doi.org/10.1201/9781003134572-04>.
- Hearty, P.J., Neumann, A., 2001. Rapid sea level and climate change at the close of the Last Interglaciation (MIS 5e): evidence from the Bahama Islands. *Quat. Sci. Rev.* 20 (18), 1881–1895. [http://dx.doi.org/10.1016/S0277-3791\(01\)00021-X](http://dx.doi.org/10.1016/S0277-3791(01)00021-X).
- Hersbach, H., Bell, B., Berrisford, P., Hirahara, S., Horányi, A., Muñoz-Sabater, J., Nicolas, J., Peubey, C., Radu, R., Schepers, D., et al., 2020. The ERA5 global reanalysis. *Q. J. R. Meteorol. Soc.* 146 (730), 1999–2049.
- Holthuijsen, L.H., 2007. Waves in Oceanic and Coastal Waters. Cambridge University Press, <http://dx.doi.org/10.1017/CBO9780511618536>.
- Janssen, P.A.E.M., 1991. Quasi-linear theory of wind-wave generation applied to wave forecasting. *J. Phys. Oceanogr.* 21 (11), 1631–1642. [http://dx.doi.org/10.1175/1520-0485\(1991\)021<1631:QLTOWW>2.0.CO;2](http://dx.doi.org/10.1175/1520-0485(1991)021<1631:QLTOWW>2.0.CO;2).
- Jinoj, T.P.S., Bonthu, S., Robin, R.S., Babu, K.K.I., Arumugam, K., Purvaja, R., Ramesh, R., 2021. Numerical modelling approach for the feasibility of shore protection measures along the coast of Kavaratti Island, Lakshadweep archipelago. *J. Earth Syst. Sci.* 130 (3), 165. <http://dx.doi.org/10.1007/s12040-021-01665-4>.
- Kalourazi, M.Y., Siadatmousavi, S.M., Yeganeh-Bakhtyari, A., Jose, F., 2021. WAVEWATCH-III source terms evaluation for optimizing hurricane wave modeling: A case study of Hurricane Ivan. *Oceanologia* 63 (2), 194–213. <http://dx.doi.org/10.1016/j.oceano.2020.12.001>.

- Karypis, G., Kumar, V., 1998. A parallel algorithm for multilevel graph partitioning and sparse matrix ordering. *J. Parallel Distrib. Comput.* 48, 71–85.
- Kodaira, T., Sasmal, K., Miratsu, R., Fukui, T., Zhu, T., Waseda, T., 2022. Uncertainty in wave hindcasts in the north atlantic ocean. <http://dx.doi.org/10.48550/ARXIV.2203.11715>.
- Koko, J., 2015. A Matlab mesh generator for the two-dimensional finite element method. *Appl. Math. Comput.* 250, 650–664. <http://dx.doi.org/10.1016/j.amc.2014.11.009>.
- Komen, G.J., Hasselmann, S., Hasselmann, K., 1984. On the existence of a fully developed wind-sea spectrum. *J. Phys. Oceanogr.* 14 (8), 1271–1285. [http://dx.doi.org/10.1175/1520-0485\(1984\)014<1271:OTEOAF>2.0.CO;2](http://dx.doi.org/10.1175/1520-0485(1984)014<1271:OTEOAF>2.0.CO;2).
- Lafage, V., Arena, F., Soares, C.G., 2015. Directional analysis of sea storms. *Ocean Eng.* 107, 45–53. <http://dx.doi.org/10.1016/j.oceaneng.2015.07.027>.
- Lafon, V., Jose, F., Tempera, F., Macedo, L., Martins, A., Santos, R.S., Bates, R., 2005. Summertime morphodynamics of two beaches presenting different wave exposure — Faial Island, Azores, Portugal. In: *Coastal Dynamics 2005*. pp. 1–14. [http://dx.doi.org/10.1061/40855\(214\)4](http://dx.doi.org/10.1061/40855(214)4).
- Li, N., Cheung, K.F., Stopa, J.E., Hsiao, F., Chen, Y.-L., Vega, L., Cross, P., 2016. Thirty-four years of hawaii wave hindcast from downscaling of climate forecast system reanalysis. *Ocean Model.* 100, 78–95. <http://dx.doi.org/10.1016/j.ocemod.2016.02.001>.
- Liau, J.-M., Roland, A., Hsu, T.-W., Ou, S.-H., Li, Y.-T., 2011. Wave refraction-diffraction effect in the wind wave model WWM. *Coast. Eng.* 58 (5), 429–443. <http://dx.doi.org/10.1016/j.coastaleng.2011.01.002>.
- Ma, Z., Liu, B., Mehra, A., Adbolali, A., van der Westhuysen, A., Moghimi, S., Vinogradov, S., Zhang, Z., Zhu, L., Wu, K., Shrestha, R., Kumar, A., Tallapragada, V., Kurkowski, N., 2020. Investigating the impact of high-resolution land-sea masks on hurricane forecasts in HWRF. *Atmosphere* 11 (9), <http://dx.doi.org/10.3390/atmos11090888>.
- Matos, A., Madeira, F., Fortes, C., Didier, E., Poseiro, P., Jacob, J., 2015. Wave energy at azores islands. In: *SCACR 2015 – 7th International Short Course and Conference on Applied Coastal Research*, 28 September – 1 October 2015, Florence, Italy..
- Mendes, D., Oliveira, T.C., 2021. Deep-water spectral wave steepness offshore mainland Portugal. *Ocean Eng.* 236, 109548. <http://dx.doi.org/10.1016/j.oceaneng.2021.109548>.
- Mentaschi, L., Voudoukas, M., Montblanc, T.F., Kakoulaki, G., Voukouvalas, E., Besio, G., Salamon, P., 2020. Assessment of global wave models on regular and unstructured grids using the Unresolved Obstacles Source Term. *Ocean Dyn.* 70 (11), 1475–1483.
- Miranda, J., Luis, J., Lourenço, N., Goslin, J., 2014. Distributed deformation close to the Azores Triple “Point”. *J. Volcanol. Geotherm. Res.* 355, 27–35.
- Mitchell, N., Beier, C., Rosin, P., Quartau, R., 2008. Lava penetrating water: submarine lava flows around the coasts of Pico Island. *Geochem. Geophys. Geosyst.* 9, 30–32.
- Mitchell, N.C., Schmidt, T., Isidro, E., Tempera, F., Cardigos, F., Nunes, J., Figueiredo, J., 2003. Multibeam sonar survey of the central Azores volcanic islands. *InterRidge News* 12, 30–32.
- Moghimi, S., Van der Westhuysen, A., Adbolali, A., Myers, E., Vinogradov, S., Ma, Z., Liu, F., Mehra, A., Kurkowski, N., 2020. Development of an ESMF based flexible coupling application of ADCIRC and WAVEWATCH III for high fidelity coastal inundation studies. *J. Mar. Sci. Eng.* 8 (5), <http://dx.doi.org/10.3390/jmse8050308>.
- Morales-Márquez, V., Orfila, A., Simarro, G., Marcos, M., 2020. Extreme waves and climatic patterns of variability in the eastern North Atlantic and Mediterranean basins. *Ocean Sci.* 16 (6), 1385–1398. <http://dx.doi.org/10.5194/os-16-1385-2020>.
- Morim, J., Hemer, M., Wang, X.L., Cartwright, N., Trenham, C., Semedo, A., Young, I., Bricheno, L., Camus, P., Casas-Prat, M., et al., 2019. Robustness and uncertainties in global multivariate wind-wave climate projections. *Nat. Clim. Chang.* 9, 711–718. <http://dx.doi.org/10.1038/s41558-019-0542-5>.
- Nguyen, V.T., Zhang, C., 2022. Assessment of the influence of TH port’s breakerwater on the hydrodynamic regime in Cua Lo and Cua Hoi Estuaries, Nghe an Province, Vietnam. In: *Feng, G. (Ed.), Proceedings of the 8th International Conference on Civil Engineering*. Springer Singapore, Singapore, pp. 46–56.
- Oliveira, T.C., Cagnin, E., Silva, P.A., 2020a. Wind-waves in the coast of mainland Portugal induced by post-tropical storms. *Ocean Eng.* 217, 108020. <http://dx.doi.org/10.1016/j.oceaneng.2020.108020>.
- Oliveira, T.C., Neves, M.G., Fidalgo, R., Esteves, R., 2018. Variability of wave parameters and Hmax/Hs relationship under storm conditions offshore the Portuguese continental coast. *Ocean Eng.* 153, 10–22. <http://dx.doi.org/10.1016/j.oceaneng.2018.01.080>.
- Oliveira, T.C., Tkalic, P., Tan, B.A., Wan, C.R., Yeo, K.P., 2020b. High-resolution wind-wave model for the sea surface wave height forecasting and hindcasting. In: *Global Oceans 2020: Singapore – U.S. Gulf Coast*. pp. 1–5. <http://dx.doi.org/10.1109/IEEECONF38699.2020.9389087>.
- Pontes, M., Athanassoulis, G., Barstow, S., Cavaleri, L., Holmes, B., Mollison, D., Oliveira-Pires, H., 1996. An atlas of the wave energy resource in Europe. *J. Offshore Mech. Arct. Eng.* 118, 307–309. <http://dx.doi.org/10.1115/1.2833921>.
- Quartau, R., Curado, F., Bouriak, S., Monteiro, J., Pinheiro, L., 2003. Projecto GEMAS - Localização e Distribuição de Areias em Redor da Ilha do Pico. Dept. Geologia Marinha, IGM, Alfragide, p. 49.
- Quartau, R., Curado, F., Cunha, T., Pinheiro, L., H.Monteiro, J., 2002. Projecto Gemas - Localização e Distribuição de Areias em Redor da Ilha do Faial. NRL Memorandum Report Tech. Rep. INGMARDEP 5/2002, Dep. Geol. Mar.-IGM, Lisboa.
- Quartau, R., Hipólito, A., Mitchell, N., Gaspar, J., Brandão, F., 2015. Comment on “Construction and destruction of a volcanic island developed inside an oceanic rift: Graciosa Island, Terceira Rift, Azores” by Sibrant et al. (2014) and proposal of a new model for Graciosa’s geological evolution. *J. Volcanol. Geotherm. Res.* 303, 146–156. <http://dx.doi.org/10.1016/j.jvolgeores.2015.07.007>.
- Quartau, R., Hipólito, A., Romagnoli, C., Casalbone, D., Madeira, J., Tempera, F., Roque, C., Chiocci, F.L., 2014. The morphology of insular shelves as a key for understanding the geological evolution of volcanic islands: Insights from Terceira Island (Azores). *Geochem. Geophys. Geosyst.* 15 (5), 1801–1826. <http://dx.doi.org/10.1002/2014GC005248>.
- Quartau, R., Tempera, F., Mitchell, N.C., Pinheiro, L.M., Duarte, H., Brito, P.O., Bates, C.R., Monteiro, J.H., 2012. Morphology of the Faial Island shelf (Azores): The interplay between volcanic, erosional, depositional, tectonic and mass-wasting processes. *Geochem. Geophys. Geosyst.* 13 (4), <http://dx.doi.org/10.1029/2011GC003987>.
- Rahimian, M., Beyramzadeh, M., Siadatmousavi, S.M., 2022. The skill assessment of weather and research forecasting and WAVEWATCH-III models during recent meteotsunami event in the Persian Gulf. *Front. Mar. Sci.* 9, <http://dx.doi.org/10.3389/fmars.2022.834151>.
- Roberts, K.J., Pringle, W.J., Westerink, J.J., 2019. OceanMesh2D 1.0: MATLAB-based software for two-dimensional unstructured mesh generation in coastal ocean modeling. *Geosci. Model Dev.* 12, 1847–1868. <http://dx.doi.org/10.5194/gmd-12-1847-2019>.
- Rogers, W.E., Babanin, A.V., Wang, D.W., 2012. Observation-consistent input and whitecapping dissipation in a model for wind-generated surface waves: Description and simple calculations. *J. Atmos. Ocean. Technol.* 29 (9), 1329–1346. <http://dx.doi.org/10.1175/JTECH-D-11-00092.1>.
- Roland, A., 2009. Development of WWM II: Spectral Wave Modelling on Unstructured Meshes (Ph.D. thesis). Technische Universität Darmstadt, Institute of Hydraulic and Water Resources Engineering, p. 212.
- Roland, A., 2012. Application of Residual Distribution (RD) schemes to the geographical part of the wave action equation. In: *Proceedings of ECMWF Workshop on Ocean Wave Forecasting*, June. ECMWF, Reading, U. K..
- Romero, L., 2019. Distribution of surface wave breaking fronts. *Geophys. Res. Lett.* 46 (17–18), 10463–10474. <http://dx.doi.org/10.1029/2019GL083408>.
- Rusu, L., Pilar, P., Guedes Soares, C., 2008. Hindcast of the wave conditions along the west Iberian coast. *Coast. Eng.* 55 (11), 906–919. <http://dx.doi.org/10.1016/j.coastaleng.2008.02.029>, Hindcast of Dynamic Processes of the Ocean and Coastal Areas of Europe.
- Rusu, L., Soares, C.G., 2012. Wave energy assessments in the Azores islands. *Renew. Energy* 45, 183–196.
- Saffir, H.S., 1973. Hurricane wind and storm surge. *Mil. Eng.* 65 (423), 4–5.
- Sandhya, K., Balakrishnan Nair, T., Bhaskaran, P.K., Sabique, L., Arun, N., Jeykumar, K., 2014. Wave forecasting system for operational use and its validation at coastal Puducherry, east coast of India. *Ocean Eng.* 80, 64–72. <http://dx.doi.org/10.1016/j.oceaneng.2014.01.009>.
- Sartini, L., Mentaschi, L., Besio, G., 2015. Evaluating third generation wave spectral models performances in coastal areas. An application to Eastern Liguria. In: *OCEANS 2015 - Genova*. pp. 1–10. <http://dx.doi.org/10.1109/OCEANS-Genova.2015.7271395>.
- Saulter, A., Bunney, C., Li, J.-G., 2016. Application of a refined grid global model for operational wave forecasting. In: *Forecasting Research, Technical Report No: 614*. <http://dx.doi.org/10.13140/RG.2.2.22242.17600>.
- Sheng, Y., Shao, W., Li, S., Zhang, Y., Yang, H., Zuo, J., 2019. Evaluation of typhoon waves simulated by WaveWatch-III model in shallow waters around Zhoushan islands. *J. Ocean Univ. China* 18 (2), 365–375.
- Simpson, R.H., Saffir, H., 1974. The hurricane disaster potential scale. *Weatherwise* 27 (8), 169.
- Soran, M.B., Amarouche, K., Akpınar, A., 2022. Spatial calibration of WAVEWATCH III model against satellite observations using different input and dissipation parameterizations in the Black Sea. *Ocean Eng.* 257, 111627. <http://dx.doi.org/10.1016/j.oceaneng.2022.111627>.
- Stopa, J.E., 2018. Wind forcing calibration and wave hindcast comparison using multiple reanalysis and merged satellite wind datasets. *Ocean Model.* 127, 55–69. <http://dx.doi.org/10.1016/j.ocemod.2018.04.008>.
- Stopa, J.E., Ardhuin, F., Babanin, A., Zieger, S., 2016. Comparison and validation of physical wave parameterizations in spectral wave models. *Ocean Model.* 103, 2–17. <http://dx.doi.org/10.1016/j.ocemod.2015.09.003>.
- Stopa, J.E., Filipot, J.-F., Li, N., Cheung, K.F., Chen, Y.-L., Vega, L., 2013. Wave energy resources along the Hawaiian Island chain. *Renew. Energy* 55, 305–321. <http://dx.doi.org/10.1016/j.renene.2012.12.030>.
- Sun, Z., Liu, X., Cai, Z., Li, J.-G., Chen, W., Ding, J., Tian, C., 2019a. A Comparison of WAVEWATCH III Grid Models for a Typical Reef Lagoon. In: *International Ocean and Polar Engineering Conference*, [arXiv:https://onepetro.org/ISOPEIOPEC/proceedings-pdf/ISOPE19/All-ISOPE19/ISOPE-I-19-227/1128279/iso-pe-i-19-227.pdf](https://onepetro.org/ISOPEIOPEC/proceedings-pdf/ISOPE19/All-ISOPE19/ISOPE-I-19-227/1128279/iso-pe-i-19-227.pdf), ISOPE-I-19-227.

- Sun, Z., Zhang, H., Liu, X., Ding, J., Xu, D., Cai, Z., 2019b. Wave energy assessment of the Xisha Group Islands zone for the period 2010–2019. *Energy* 220, 119721.
- Swain, J., P. A., U., Balchand, A., 2017. Wave hindcasting using WAM and WAVEWATCH III – A comparison study utilizing Oceansat-2 (OSCAT) winds. *J. Oceanogr. Mar. Res.* 5, 9. <http://dx.doi.org/10.4172/2572-3103.1000166>.
- Tempera, F., 2008. Benthic Habitats of the Extended Faial Island Shelf and their Relationship to Geologic, Oceanographic and Infralittoral Biologic Features (Ph.D. thesis). School of Geography and Geosciences, University of St. Andrews, p. 311.
- Tolman, H.L., 2008. A mosaic approach to wind wave modeling. *Ocean Model.* 25, 35–47.
- Tolman, H.L., Chalikov, D., 1996. Source terms in a third-generation wind wave model. *J. Phys. Oceanogr.* 26 (11), 2497–2518. [http://dx.doi.org/10.1175/1520-0485\(1996\)026<2497:STIATG>2.0.CO;2](http://dx.doi.org/10.1175/1520-0485(1996)026<2497:STIATG>2.0.CO;2).
- Tozer, B., Sandwell, D.T., Smith, W.H.F., Olson, C., Beale, J.R., Wessel, P., 2019. Global bathymetry and topography at 15 arc sec: SRTM15+. *Earth Space Sci.* 6 (10), 1847–1864. <http://dx.doi.org/10.1029/2019EA000658>.
- Umesh, P., Behera, M.R., 2020. Performance evaluation of input-dissipation parameterizations in WAVEWATCH III and comparison of wave hindcast with nested WAVEWATCH III-SWAN in the Indian Seas. *Ocean Eng.* 202, 106959. <http://dx.doi.org/10.1016/j.oceaneng.2020.106959>.
- Violante-Carvalho, N., Arruda, W.Z., Carvalho, L.M., Rogers, W.E., Passaro, M., 2021. Diffraction of irregular ocean waves measured by altimeter in the lee of islands. *Remote Sens. Environ.* 265, 112653. <http://dx.doi.org/10.1016/j.rse.2021.112653>.
- Waseda, T., Sasmal, K., Kodaira, T., Kita, Y., Miratsu, R., Zhu, T., Fukui, T., 2021. Modeled and satellite-derived extreme wave height statistics in the North Atlantic Ocean reaching 20 m. *Earth Space Sci. Open Arch.* 18. <http://dx.doi.org/10.1002/essoar.10506278.1>.
- Wu, Z., Chen, J., Jiang, C., Deng, B., 2021. Simulation of extreme waves using coupled atmosphere-wave modeling system over the South China Sea. *Ocean Eng.* 221, 108531. <http://dx.doi.org/10.1016/j.oceaneng.2020.108531>.
- WW3DG, 2019. User Manual and System Documentation of WAVEWATCH III Version 6.07, The WAVEWATCH III Development Group. Tech. Note 326 Pp. + Appendices, NOAA/NWS/NCEP/MMAB.
- Yang, Z., Shao, W., Ding, Y., Shi, J., Ji, Q., 2020. Wave simulation by the SWAN model and FVCOM considering the sea-water level around the Zhoushan islands. *J. Mar. Sci. Eng.* 8 (10), 783. <http://dx.doi.org/10.3390/jmse8100783>.
- Zelinsky, D., 2019. National Hurricane Center Tropical Cyclone Report Hurricane Lorenzo. Rep. AL132019, National Hurricane Center.
- Zieger, S., Babanin, A.V., Erick Rogers, W., Young, I.R., 2015. Observation-based source terms in the third-generation wave model WAVEWATCH. *Ocean Model.* 96, 2–25. <http://dx.doi.org/10.1016/j.ocemod.2015.07.014>, Waves and coastal, regional and global processes.